High Efficiency Thin Film CdTe and a-Si Based Solar Cells

Annual Technical Report for the Period
March 4, 1999 to March 3, 2000

Contract No. ZAF-8-17619-14

Alvin D. Compaan, principal investigator
Xunming Deng, co-principal investigator
Randy G. Bohn, co-investigator

NREL technical monitor: B. von Roedern

Department of Physics and Astronomy
The University of Toledo
Toledo, OH 43606

SUMMARY

This report covers the second year of this subcontract for research on high efficiency CdTe-based thin-film solar cells and on high efficiency a-Si-based thin-film solar cells. The effort on CdTe-based materials is led by Prof. Compaan and emphasizes the use of sputter deposition of the semiconductor layers. The effort on high efficiency a-Si materials is led by Prof. Deng and emphasizes plasma-enhanced chemical vapor deposition for cell fabrication with major efforts on triple-junction devices.

Major accomplishments for the CdTe group over the past year include the following:

- Implemented a diode-array spectrograph system and utilized optical emission spectroscopy to help optimize the reactive sputtering of N-doped ZnTe for CdTe back contact structures.
- Identified the photoluminescence signatures of various defect states in CdTe related to Cd vacancies, Cu_{Cd} acceptors, Cu-V_{Cd} complexes and donor-acceptor pairs, and related these states to instabilities in the hole concentration at room temperature.
- Showed that Cu is an important non-radiative center in CdS, reducing the PL efficiency.
- Studied band tailing in CdS weakly alloyed with CdTe and CdTe weakly alloyed with CdS.
- Fabricated superstrate ITO/CdS/CdTe cells on Mo substrates with efficiencies above 7.5%.
- Collaborated in studies of EXAFS of Cu in CdTe which indicate a Cu-Te bond length of 2.62 A or 6.7% shorter than the CdTe bond in agreement with calculations of Wei, et al.
- Provided assistance to two groups on laser scribing.

Major accomplishments for the a-Si group over the past year include the following:

- Comparatively studied the performance of a-SiGe solar cells and properties of a-SiGe single layer films deposited using a wide range of H dilution, observed transition from a-SiGe to μc-SiGe at high H dilution and the impact on cell performances
- Comparatively studied the performance of a-SiGe solar cells and properties of a-SiGe single layer films with different Ge contents, suitable for use as component cells of triple-junction devices
- Fabricated a-Si based solar cells on ultra-thin stainless steel substrate (7.5 micron) and obtained equivalent performance and yield as on the regular SS substrates (127 micron)
- Comparatively studied the performance of a-Si based solar cells on SS substrates and on SnO_2-coated glass substrates.
- Studied the performance of p-layers deposited under various deposition conditions for n-i-p type solar cells.
- Performed an analysis for the component cell current matching within a triple-junction solar cell.

TABLE OF CONTENTS

LIST OF FIGURES

LIST OF TABLES

1 Introduction

1.1 Background

This annual report covers the second year of the current NREL thin-film partnership subcontract with the University of Toledo which supports cell fabrication and related materials studies on two types of thin-film solar cells, CdTe-based and a-Si:H-based.

1.2 Technical Approach

1.2.1 Cadmium Telluride-Based Cells

Magnetron sputtering—Our CdTe-based effort is focused on the use of rf sputtering for thin film deposition. Much of our effort is designed to exploit the effects of excited state species in the plasma to improve the film growth or lower the growth temperature. The ultimate goal is to fabricate rf sputtered CdS/CdTe thin film solar cells with efficiencies exceeding 15% on soda-lime glass. For the CdS and CdTe deposition, we utilize a specially designed two-gun magnetron sputtering chamber with optical thickness monitors as described previously. A second, similar sputtering chamber is used for deposition of contact structures. In this chamber we presently do reactive sputtering of ZnTe:N. This is one example of utilizing the energy in the sputtering plasma, in this case to dissociate N_2 to make atomic N available for electrically-active incorporation in the film. A third sputtering system is used to extend the range of metals available for contact structures. This dc magnetron sputtering system has been used for the deposition of Ni on top of the ZnTe:N layers.

Pulsed Laser Deposition (PLD)--We have continued to make limited use of PLD as a convenient method for preparation of films with unusual composition. Thus we have prepared additional films of the ternary alloy CdS_xTe_{1-x} and bilayers of CdS/CdTe for synchrotron-based experiments with collaborators at the Univ. of Buffalo.

Post-Deposition Processing—For post-deposition processing of the sputtered films we have now standardized on a vapor $CdCl_2$ treatment and can handle substrate sizes of about three-inch square.

1.2.2 Amorphous-Silicon-Based Cells

Triple-cell fabrication—One of our focused efforts is to fabricate high efficiency triple-junction a-Si based solar cells. A plasma-enhanced chemical vapor deposition (PECVD) process is used for the deposition of all semiconductor layers. In addition, this year we have completed the construction of a novel hot-wire deposition system which is accessible from the central load lock together with the two PECVD chambers. Our efforts include the optimization of a-Si and a-SiGe intrinsic layers with improved network ordering, optimization of doped microcrystalline silicon p-layers and amorphous silicon n-layers, optimization of tunnel junctions and interfaces. The goal is to achieve 12.5% stable solar cells (total area) at the end of Year 3.

Novel processes for high quality narrow-bandgap a-SiGe deposition—Various approaches are used to explore the deposition of narrower-bandgap (~1.3 eV) a-SiGe materials. We have completed the installation of the hot-wire chamber which includes a special design to make a-SiGe alloys with several different gas flow patterns for Si_2H_6, GeH_4 and H_2 gases.

Non-semiconductor layers—We also optimize the deposition of ITO and other non-semiconductor layers which are required for the solar cell operation. Interfaces between semiconductor and the non-semiconductor layers, ITO top electrodes and ZnO back-reflector, are being explored.

1.2.3 Characterization Tools

For characterization of films and cells, we continue to use SEM, EDS, x-ray, Raman, photoluminescence, optical absorption, Hall measurements, C-V, I-V, and SQE. We have continued collaborative efforts with Case Western Reserve University for Rutherford Backscattering and XPS measurements, electroluminescence measurements with the University of North Carolina, mobility-lifetime measurements with UCLA, and synchrotron x-ray measurements with the University of Buffalo and Brookhaven National Lab, and ellipsometry with Brooklyn College (CUNY).

1.2.4 Laser Scribing

We continue to maintain facilities for making laser scribes on substrates up to ~6 inch square. Scribing can be done, at either the 1064 nm or 532 nm lines, with a cw-lamp-pumped repetitively Q-switched Nd:YAG or a flash-lamp-pumped Nd:YAG. In addition, we can use the XeCl laser at 308 nm. In the past year we have used these scribing facilities for work on submodules of our sputtered cells and for some collaborative work at the request of other groups.

2. Cadmium Telluride-Based Cells and Materials

2.1 Instrumentation improvements

During Phase II of this project we were able to utilize productively some of the instrumentation advances made possible with the support for capital equipment purchases during Phase I. Thus we have relied heavily on the Dektak[3] profilometer for film thickness measurements and on the solar simulator acquired last year. Supplemental vacuum equipment was also very valuable. One of the acquisitions was a system for absorption and emission spectroscopy of gas-phase and vapor phase constituents. An example of its use is provided in Section 2.1.1. In addition, smaller equipment projects during the year have enhanced our capabilities. These include the construction of a Peltier-cooled system for variable-temperature I-V measurements and construction of a two-inch sputter-target press for use at elevated temperatures. The target press and I-V-T system are described in Sections 2.7 and 2.8, respectively.

2.1.1 Emission spectra of sputter plasmas

Early in this phase we completed assembling the system for studying optical emission and absorption from sputtering and CVD plasmas. It consists of a 0.48 m spectrograph from CVI Laser, a 1024 element photodiode array from Roper Scientific, and a xenon arc lamp from Photon Technologies. The photodiode array was chosen over a conventional CCD specifically for its 22-bit dynamic range, to extend its utility in absorption spectroscopy. The system has a wavelength resolution of better than one angstrom, with a range of 190 – 800 nm.

As an example of the use of this system we show the results of our study of the nitrogen species present in the plasma during reactive sputtering of ZnTe films with partial pressures of N_2. For the observations of sputtering conditions, we imaged the region of highest plasma density just above the sputter cathode into the end of the fused silica optical fiber which relayed the light into the spectrometer. For sputter gas pressures in the range from 10 to 30 mTorr, we observed significant amounts of both neutral (N_2) and ionized (N_2^+) molecular nitrogen. However, we have not yet observed emission lines from atomic N in the sputter gas.

To determine the effect of deposition parameters on the nitrogen species, we monitored the ratio N_2^+/N_2 for various conditions. Shown in Figure 2-1 are spectra for 5% N_2 in Ar sputtering gas at pressures of 10 mTorr and 30 mTorr. Note that the 391.4 nm N_2^+ line increases in intensity at lower pressures, while the 399.8 nm N_2 line decreases. [The 391.4 nm N^+ line originates from the transition $B\ ^2\Sigma_u^+ \rightarrow X\ ^2\Sigma_g^+$ ($\nu'=0 \rightarrow \nu''=0$) with an upper state at about 18.5 eV. The 399.8 nm line of N_2 orginates from the transition $C\ ^3\Pi_u \rightarrow B\ ^3\Pi_g$ ($\nu'=1 \rightarrow \nu''=4$) with an upper state at about 11 eV.][1] As expected, increased ionization occurs at low pressures because of increased electron mean free path and therefore an increased hot electron tail which is most important for ionizing collisions.

Table 2 shows the ionization ratio and resistivity for ZnTe:N films grown under various conditions. Samples A-C show the effect of sputtering pressure – the ionization of molecular nitrogen decreases monotonically from 10 to 30 mTorr. The lowest resistivity film is grown at 20 mTorr. Samples D and E indicate that higher sputter gas flow rates result in lower film resistivities, although there is no appreciable change in nitrogen ionization at the sputter target

with flow rate. These results suggest that film resistivity of ZnTe reactively sputtered with N_2 in Argon may be determined by the supply of activated N_2 to the growing film/plasma interface.

The absence of detectable levels of *atomic* nitrogen in the plasma is surprising. Groups using plasma-source nitrogen in MBE typically report a strong correlation with the amount of atomic nitrogen present in the plasma.[2] We have also tried using NH_3 instead of N_2 for the reactive sputter doping of ZnTe; however, the doping level as measured by the conductivity was about an order-of-magnitude less. It is possible that hydrogen incorporation may be limiting the doping level, but we have as yet no direct evidence of this. Therefore, for subsequent work we have returned to the use of N_2/Ar mixtures. Cell performance with the use of ZnTe:N for back contact buffer layers is described in the next section.

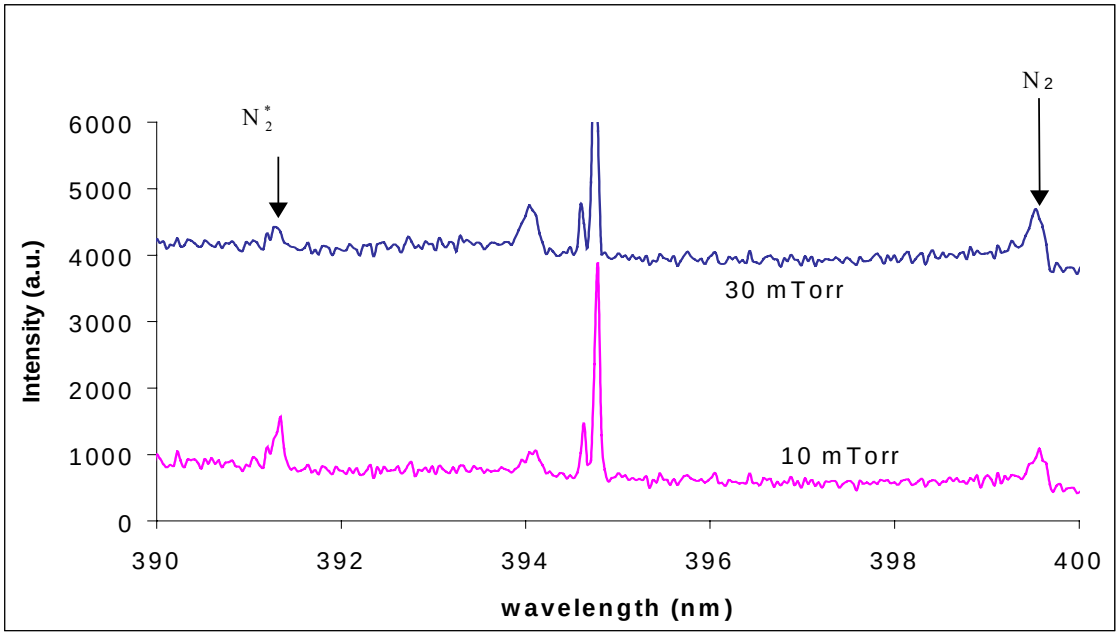

Figure 2-1: Plasma emission from Ar/N_2 sputtering plasma at 10 and 30 mTorr. Upper trace is shifted vertically by 3300 units.

Table 2-1. Nitrogen ionization and ZnTe:N film resistivity for various conditions

Sample	A	B	C	D	E
N_2/(Ar+ N_2)	3.1%	3.1%	3.1%	2.25%	2.25%
Flow rate (sccm)	50	50	50	18	72
Pressure (mTorr)	10	20	30	20	20
N_2^+ /N_2	1.2	0.57	0.41	0.59	0.59
Resistivity (ohm-cm)	150	86	370	175	50

2.2 Studies of reactively sputtered ZnTe:N for back contact applications

2.2.1 Carrier concentration and mobility

In our Phase 1 Annual Report, we presented results on reactively sputtered ZnTe films doped with nitrogen. During Phase 2 we have made some improvement in the magnetron sputtering system by providing for gas injection at the sputter gun in addition to the former location at the edge of the sputter chamber relatively far from the magnetron. This has yielded slight improvement in the doping concentrations and more reproducible results. In addition, we have succeeded in obtaining Hall measurements of the doped films by growing thicker layers. The results of the Hall measurements are shown below. We observe some unusual behavior in the spatial variation in the film electrical parameters. The center of the film which is positioned directly 70 mm across from the center of the 50 mm diameter sputter gun is more resistive than the edges, approximately 40 mm from the film center. The film edge has about half the thickness of the center but has actually *lower* sheet resistance. Carrier concentration is about four times higher at the edge, although mobility is lower by almost a factor of two. The lower mobility would be consistent with increased ionized impurity scattering but the the carrier concentrations are really too low to explain this. We believe that grain size and/or morphology may explain some of this behavior. This dependence on location relative to the sputter gun hopefully will provide us an opportunity to improve our understanding of the doping process and allow achievement of even higher doping levels.

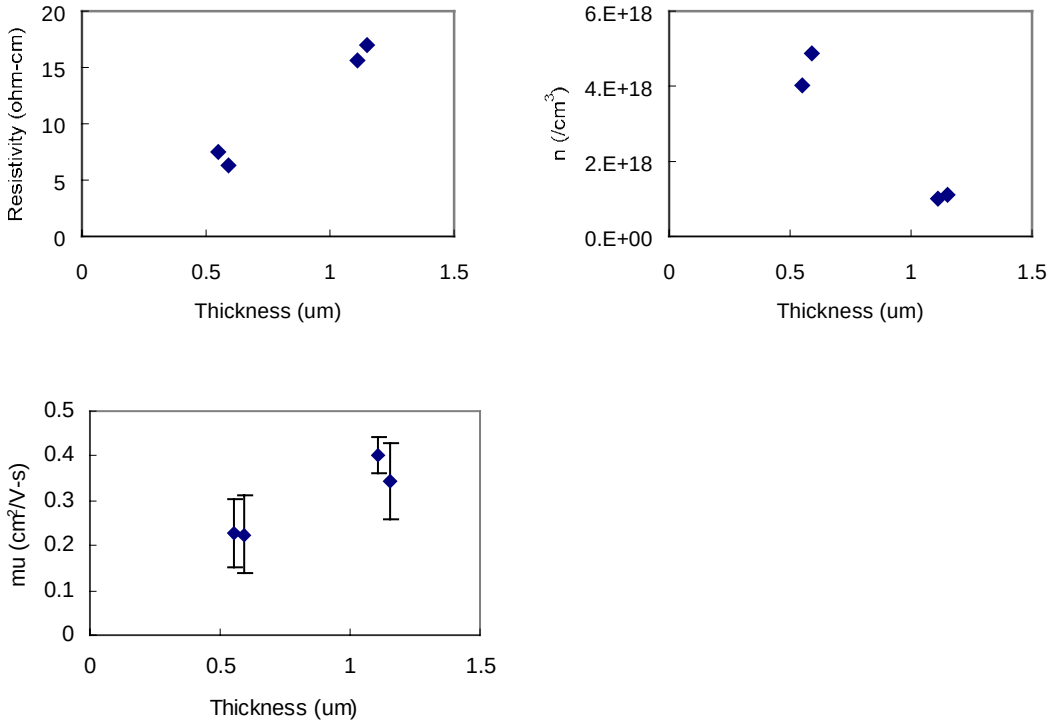

Fig. 2-2. Hall measurement results on reactively sputtered ZnTe:N film from two locations near the center (1.2 μm thickness) and two near the edge (0.6μm). The errors in resistivity are about ±5% and about ±30% in carrier concentration and mobility, largely due to the low μ.

Both the undoped and the doped ZnTe films show good transparency as indicated in Fig. 2-3 below. These data represent "specular" transmission, obtained without the use of an integrating sphere. The film roughness is low as shown by the strong interference fringes and we believe that most of the transmission loss at the peaks is due to residual absorption. It should be noted that the data of Fig. 3 are from relatively thick films (~1μm) in comparison to the typical

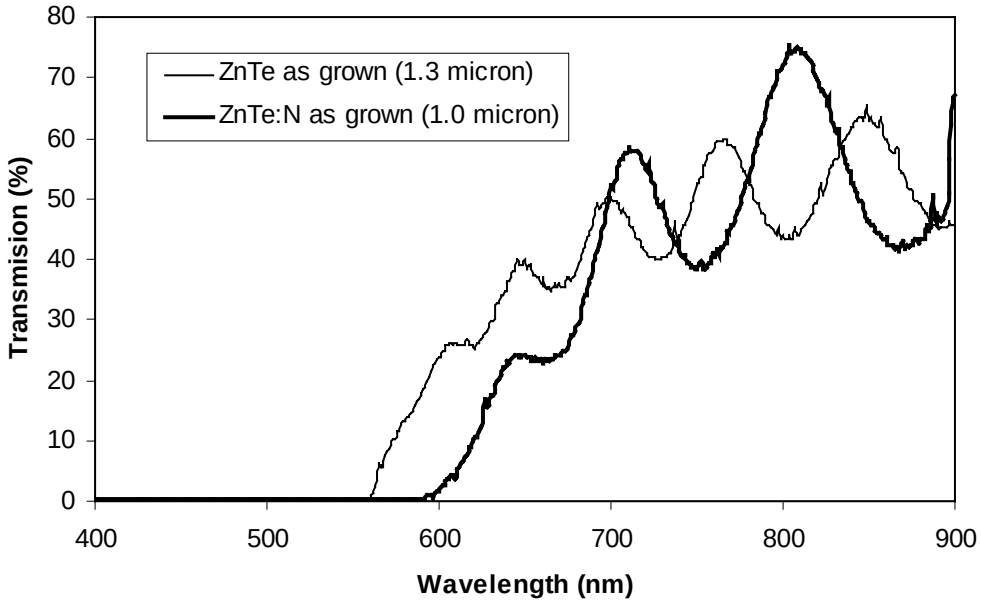

thickness of 0.14 μm which we have used in the contact structures described below.

Fig. 2-3. Specular transmission of undoped and N-doped ZnTe films on glass

2.2.2 Stability studies of cells with ZnTe:N back contact buffer layers

Early results of the use of the reactively sputtered ZnTe:N in back contact structures were provided in the last annual report. Xianda Ma, whose M.S. thesis was completed in May, 1999, was able to obtain lateral resistivities as low as 5 Ω-cm in thin films on borosilicate glass and furthermore was able to fabricate ZnTe/ZnTe:N/Ni contacts on First Solar material which yielded cell efficiencies near 10%. These contacts, with no intentional copper, showed lower than usual open-circuit voltage and somewhat lower fill factors. During the past year more extensive stability studies of these contacts were performed and data are reported here.

Stress testing of the first of these ZnTe:N-based contact structures was done at both First Solar, LLC, and UT. The UT work was done by post-doc Kent Price and a 1999 summer intern, David Simmons, who participated in our group through an NSF-sponsored Research Experiences for Teachers program. (See discusion of the NSF-RET program below.) In the table below, we present some of the results on these cells stressed. Our test results were qualitatively similar to those of First Solar. However, because of ELH lamp changes our cell currents were not well controlled between measurements and most of the currents are high.

Identical CdTe solar cell "plates" were obtained from First Solar. These were finished at First Solar including $CdCl_2$ procesing, but had no back interfacial or contact layer. We used two different contacting schemes for the study. One set of cells received UT's "standard" back contact of 40 Å Cu and 200 Å Au, deposited by thermal evaporation, followed by a 45 minute

diffusion at 150 C. The other set of cells received a copper-free back contact of a sputter-deposited 50 nm layer of ZnTe, a 100 nm layer of ZnTe:N, and 300 nm of DC-sputtered Ni. This was followed by a 45 minute diffusion at 200 C in air. Samples were I-V tested at one sun immediately after preparation, before any light soak. The cells were kept at indoor ambient temperature and lights for 60 days before the stressing was initiated. Just before stressing, the substrates (with many cells each) were cut into individual cells to provide samples for stress-testing under various conditions.

The following conditions were used:

1. A control cell of each contact type remained at ambient temperature and light,
2. Two cells of each type were baked at 100-110 C in the dark
3. One cell of each contact type was light-soaked at one sun under resistive load at approximately maximum power (MP). The equilibrium temperature was ~60 C.
4. One cell of each contact type was light-soaked under one sun at V_{OC}, 60 C.

A summary of the results of the stability testing is provided in Table 1, listing initial and final efficiency, V_{oc}, I_{sc}, and fill factor, as well as the stress condition and time.

The unstressed, control cells, "A" showed small changes in efficiency. The Cu/Au contacted cells had generally higher initial efficiencies, typically near 9.9% while the ZnTe:N/Ni cells had initial efficiencies of around 9.7%. The increased efficiency is due to a higher V_{oc}, presumably due to the doping effects of Cu in the CdTe. Over a period of about five months the efficiency of the unstressed Cu/Au cells had dropped to 8.3% while the ZnTe:N/Ni cells degraded to 8.5%. Our cell currents, however, have relatively large uncertainties due to instability in the ELH lamps and lamp-to-lamp variability. The light source now has been replaced with an Oriel solar simulator. The Cu/Au cell experienced a more significant decline in both V_{oc} and FF. This is consistent with a month-long shelf stability test reported in our most recent annual report. In that study, V_{oc} and FF decreased in the cell with copper-based contacts, but not in the ZnTe:N-contacted cell.

The two sets of cells stressed under "hot/dark" conditions in air, "B" & "C", exhibited considerable differences between the Cu/Au and the ZnTe:N/Ni contacts. Initial efficiencies for these cells were approximately 9.5% for each sample. After baking, the efficiency of three of the cells dropped to 7.6 – 7.9%, while that of Cu/Au B dropped to 4.4%. The decrease in the ZnTe:N efficiency was caused by a decrease in both V_{oc} and I_{sc}, while the fill factor was stable. The Cu/Au cells actually experienced an increase in V_{oc} of about 40 mV, but a significant decrease in I_{sc} and FF.

The third set of cells, "D" were stressed under one-sun light-soaking, 60 C, at V_{MP} for 1200 h. After stressing, the ZnTe:N contacted cell showed slightly higher performance than the Cu/Au contacted cell although the Cu/Au contact was significantly better at the beginning.

The fourth set of cells, "E", were stressed under one-sun light-soaking at V_{OC} for 1200 h. In this case, again, there was some deterioration in the parameters for both types of contacts. However, there was much less deterioration for the ZnTe:N contacted cell.

Together, these stability tests reveal some interesting trends. Initially, the average efficiency is higher for the Cu/Au cells (9.9%) than for the ZnTe:N cells (9.6%), but the final efficiency averaged over all the stress conditions is lower for the Cu/Au contacts (6.8% compared to 7.8%). I_{sc} degraded significantly for all of the studied cells, and we believe this is partially due to a change in the lamp that was used for the I-V characterization. Initial V_{oc} is higher for the Cu/Au cell than the ZnTe:N cell in every set. V_{oc} is stable in the ZnTe:N cell that remained in room ambient conditions, but degraded for all stressed ZnTe:N cells. On the other hand, the V_{oc} degraded of the Cu/Au cells that remained either in room-ambient conditions or were light-soaked, while V_{oc} of the Cu/Au dark, heat-stressed cell increased. The behavior of V_{oc}

in the Cu/Au cells is consistent with the work of Dan Grecu.[3,4,5] Dan has shown via photoluminescence that metastable Cu-related defects form in Cu-doped CdTe that has been aged at room temperature or exposed to white light. These defects lower the CdTe carrier concentration and V_{oc}. Furthermore, an anneal at elevated temperatures can reverse defect formation and restore V_{oc}, just as is observed in the current study.

Table 2-2. Characteristics of Cu/Au and ZnTe:N contacted First Solar material immediately after contacting, immediately before stressing, and after stressing (UT data)

Contact	Stress condition	'Stress Time	Eff. (%)	Voc	Isc	FF
ZnTe:N A	initial		9.65	0.732	4.21	56.5
	unstressed	146 days	8.5	0.732	3.77	55.9
Cu/Au A	initial		9.9	0.784	3.58	64.1
	unstressed	146 days	8.3	0.749	3.32	60.2
ZnTe:N B	initial		9.7	0.736	4.12	58.0
	unstressed	60 days	9.3	0.759	4.02	55.1
	100C/dark	1200 h	7.8	0.713	3.55	55.9
Cu/Au B	initial		9.6	0.788	3.58	61.7
	unstressed	60 days	9.2	0.786	3.47	61.0
	100C/dark	1200 h	4.4	0.836	3.07	31.0
ZnTe:N C	initial		9.6	0.738	4.02	58.4
	unstressed	60 days	10.2	0.756	4.02	60.8
	100C/dark	1200 h	7.95	0.699	3.51	58.7
Cu/Au C	initial		9.3	0.791	3.56	59.7
	unstressed	60 days	9.3	0.792	3.49	60.8
	100C/dark	1200 h	7.64	0.822	3.37	49.9
ZnTe:N D	initial		9.7	0.742	4.15	56.9
	unstressed	60 days	11.7	0.741	4.43	64.5
	60C/soak/MP	1200 h	7.15	0.689	3.24	54.8
Cu/Au D	initial		10.1	0.8	3.56	63.9
	unstressed	60 days	9.1	0.765	3.64	59.5
	60C/soak/MP	1200 h	7	0.765	3.14	52.8
ZnTe:N E	initial		9.2	0.751	4.06	54.5
	unstressed	60 days	10.4	0.749	4.10	61.5
	60C/soak/OC	1200 h	7.77	0.716	3.32	59.2
Cu/Au E	initial		10.5	0.802	3.67	64.0
	unstressed	60 days	9.4	0.762	3.68	60.8
	60/C/soak/OC	1200 h	6.6	0.741	3.15	51.4

It is therefore not surprising that for the nominally Cu-free, ZnTe:N contacted cells, V_{oc} behaves differently under room-ambient and elevated temperature stress. Fill factor also changed differently in the two types of cells. In the ZnTe:N cells, fill factor was quite stable, never decreasing by more than 2.1 units or percent absolute (although for sample D there was an intermediate increase by 7.6 units in FF with 60 days of room temperature storage), and in case E increasing by 4.7 units after 60 days of room temperature storage and followed by the 1200 h of

light soak. However, in the Cu/Au cells FF degraded by at least 4 in every case, and averaged more than 10 units.

These results should be considered preliminary due to the extended interval after fabrication before the stress-testing began and due to the uncertainty introduced by the change in lamps. Further study clearly is merited to elucidate how degradation mechanisms differ in cells containing copper and those without intentional copper, and to continue to improve the efficiency of the ZnTe:N-contacted cells.

Other reproducibility difficulties appear to be related to the details of the preparation of the CdTe surface. This may very well relate to the lack of any intentional doping of the CdTe surface in this contact structure (glass/TCO/CdS/CdTe/ZnTe:N/Ni). We are simultaneously working on achieving some plasma-doping of CdTe with N and other elements. We have found some evidence of doping of CdTe with N_2/Ar sputter gas mixtures but so far the doping limits of CdTe with N appear to be several orders of magnitude lower than for ZnTe. We are convinced that high quality and reproducible ZnTe:N-based contacts will require advances in the doping of the back surface of CdTe.

As noted on p. 2-5 above, the ZnTe-based contacts were fabricated with an undoped buffer layer between the CdTe and the doped ZnTe. We are presently studying whether and how much undoped ZnTe is necessary for a good contact and to what extent this buffer layer may affect the cell stability.

2.3 Cu in CdS/CdTe solar cells

In Phase II, Dan Grecu finished his Ph.D., and we have been following up his work which emphasized PL studies in single crystal and polycrystalline films. We have conducted a series of experiments to examine similar effects of Cu in CdS. We have also started a collaboration with Gerardo Contreras of the Polytechnic Institute of Mexico City to study the diffusion of Cu by PL in 100 μm thick films of CdTe grown by closed space sublimation and in 1 mm thick single crystals. This work is partially funded by the NSF through their International Programs Division and by the CONACyT agency of Mexico.

Related to this work with copper-doping in CdTe, we performed some inductively coupled plasma spectroscopy (ICP) studies of Cu in films and source materials CdTe, ZnTe, and $CdCl_2$. For example the manufacturer's data indicated 2 ppm of Cu in $CdCl_2$ and our ICP tests showed 0.1 ppm. Some residual Cu was identified in all three source materials but it appears to be below levels which would cause concern.

2.3.1 Aging Effects in Cu-doped, single-crystal CdTe

This section has been excerpted from a manuscript which is scheduled to appear in the September 1, 2000, issue of the Journal of Applied Physics.[6] It represents follow-on work to the Ph.D. dissertation of Dan Grecu and was done in collaboration with David Young of NREL, and with Doug Rose and Upali Jayamaha of First Solar, LLC. Further background, discussion, and details can be found in the J. Appl. Phys. manuscript.

It has been reported that CdTe samples doped with Ag and Cu[7] as well as other impurities[8] show decay in the carrier concentration and changes in the photoluminescence (PL) spectrum after storage at room temperature. This aging behavior was generally attributed to the instability of the metal substitutional acceptor state on the Cd lattice site M_{Cd} (M= Ag, Cu) and formation of complexes of the type cadmium vacancy-metal interstitial (V_{Cd}-M_i) and/or M_{Cd}-M_i.[8] The tendency of noble metals to form complex states in CdTe was suggested by various experimental methods.[9] It was observed that aged Ag-doped CdTe could recover optical and electrical properties after re-annealing.

In the case of Cu-doped CdTe samples, we find that the intensity of Cu-related features in the PL spectrum decreases substantially after several days of room-temperature storage for both single crystal and polycrystalline samples. We also observe a decrease in the carrier concentration in polycrystalline CdTe films and a drop in the open-circuit voltage of the CdS/CdTe solar-cell devices doped with Cu when stored in the dark at room temperature. The aging effect appears to be accelerated by exposing the samples to white-light radiation.

However, the Cu/Au contacted cells heat stressed in the dark (B & C) showed increases in V_{oc}. Similarly, we find that, just as in the case of Ag, the PL spectrum and the carrier concentration can be restored by re-annealing the samples.

Figure 2-5 illustrates the changes in the PL signal for a Cu-doped single crystal CdTe sample (1) immediately after diffusion (30 min., 200°C), (2) after 90 hours of illumination ($2000 W/m^2$) at room temperature and (3) after a re-anneal (30 min., 200°C). The illumination of the sample was achieved using a tungsten-halogen incandescent light source. In the "aged" sample we note a significant overall decrease of the PL signal including the intensities of the 1.45 eV band, the 1.59 eV bound exciton, and the complex line at 1.555eV. These aging effects are consistent with the dissociation of Cu_{Cd} and Cu_i^+-V_{Cd}^- states discussed previously. In addition, we attribute the overall decrease in the PL signal to the formation of Cu-related non-radiative recombination centers (possibly Cu precipitates[7]). Similar samples stored in the dark

at room temperature exhibit similar but less pronounced PL degradation. Some degree of variability was observed in the aging behavior of single-crystal samples obtained from different vendors. Note that these anneals and light soaks were carried out in air.

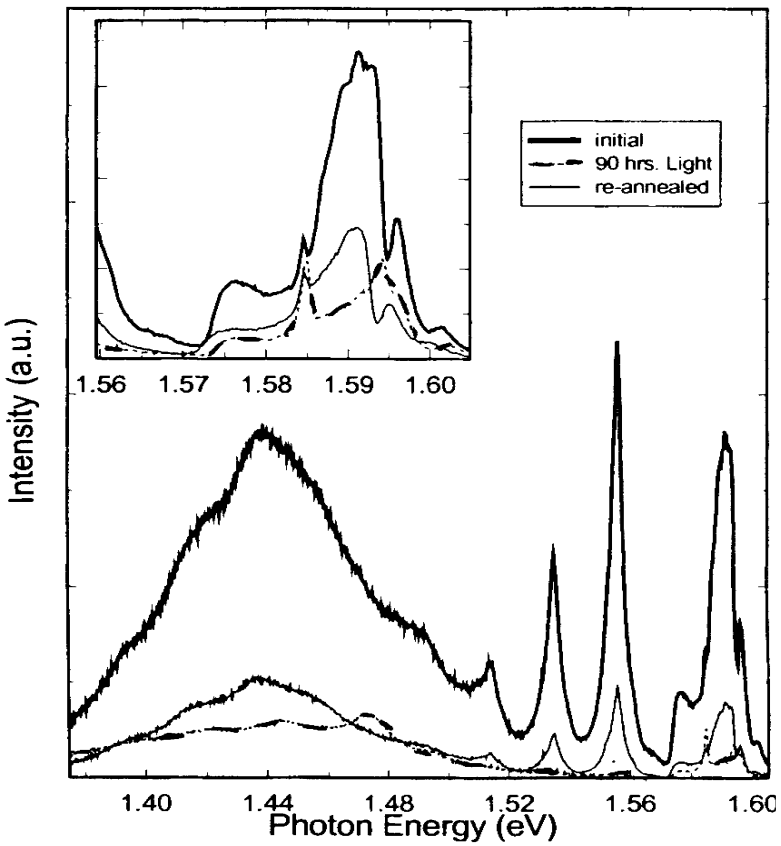

Fig. 2-5. PL of CdTe:Cu immediately after diffusion, after 90 hr light exposure, and after re-anneal.

Annealing the samples in a Cd or Te overpressure had a dramatic influence on the Cu-related aging behavior. We observe that samples annealed with Cu in a Cd overpressure show a substantially amplified PL degradation when compared with similar samples annealed in a Te overpressure as illustrated in Figure 2-6. For the Cd-annealed sample the amplitude of the bound-exciton region of the spectrum drops by a factor of 2-3 and undergoes an apparent shift towards higher energies. This shift is due to the drop in intensity of the 1.59 eV exciton-bound to Cu_{Cd} relative to bound exciton transitions at higher energies. In addition, the 1.45 eV DAP band exhibits a drop of 6000 times. In contrast, the Te-annealed sample exhibits a relatively constant overall luminescence signal although it is much weaker than for the Cd-annealed sample. A shift towards higher energies of the 1.555 eV line is clearly noticeable, and presumably due to changes in the Cu-V_{Cd} complexes.

The intensity decrease of the Cu_{Cd} related PL transitions in samples annealed in a Te overpressure (Fig. 2-6a) relative to samples annealed in a Cd overpressure (Fig. 2-6b) is indicative of the important role played by the Cd vacancies in "stabilizing" Cu atoms in the CdTe lattice. We suggest that, while Cu_{Cd} states are likely to dissociate at a similar rate regardless of

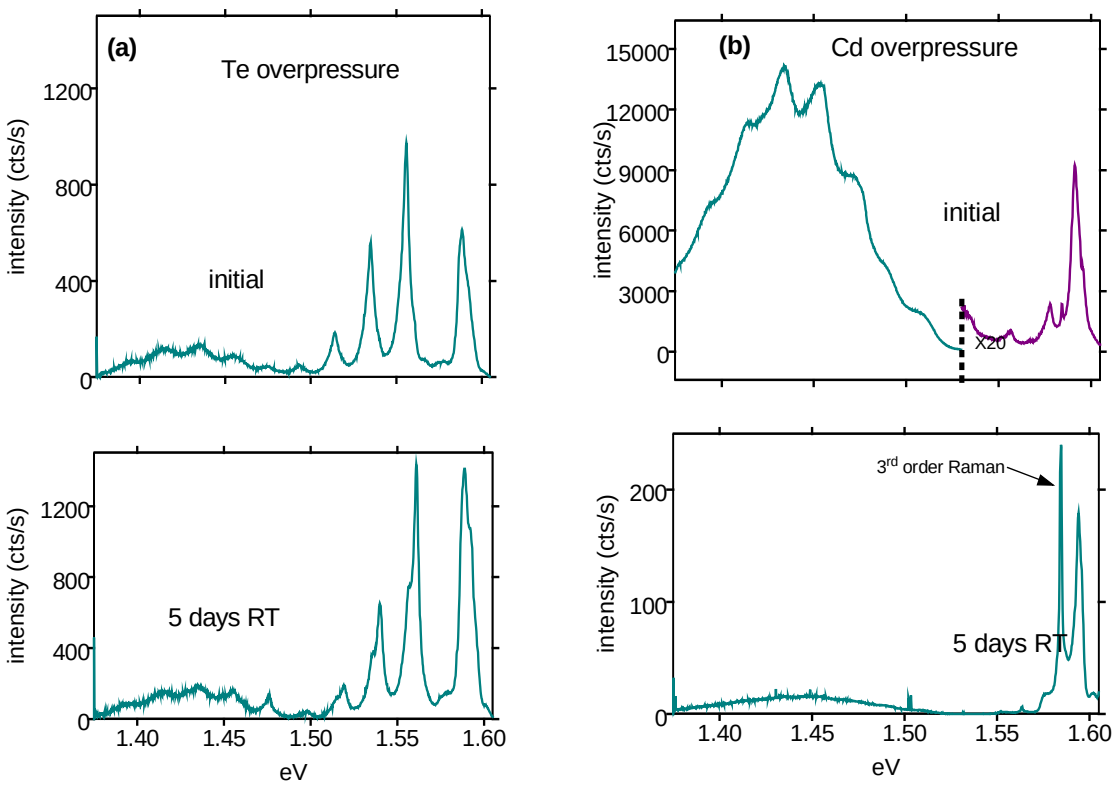

Fig. 2-6 PL from single crystal CdTe at 10 K excited at 752 nm. Two different pieces from the same crystal but annealed a) in Te overpressure and b) in Cd overpressure.

the density of Cd vacancies, a diffusing Cu_i^+ ion has a higher probability to recombine with a new V_{Cd}^- in the sample with an increased number of Cd vacancies. In the absence of the Cd vacancies, Cu ions are more likely to precipitate or otherwise participate in the formation of non-radiative recombination centers.

The dissociation of Cu acceptor states, as indicated by the PL data, was confirmed by Hall measurements on polycrystalline Cu–doped CdTe films. The results show a drop in the carrier concentration of "aged" samples which is recoverable by a heat treatment. A series of measurements separated by seven-day intervals were performed and the results are summarized in Table 2-3 (all measurements performed at room temperature). It can be seen that the carrier concentration, similar to the PL intensity, has a metastable behavior. Immediately after an anneal the measured carrier concentration is approximately 5-6x10^{14} cm^{-3}. Similar carrier concentrations in the CdTe layer were observed in solar-cell devices with a Cu-doped ZnTe back-contact (2% Cu)[10] and Cu/Au back contacts.[11] After seven days storage, the carrier concentration drops by a factor of 5-10. This effect is consistent with the dissociation/neutralization of Cu-related acceptor states suggested by the PL results. A similar drop in carrier concentration was recently reported by Hiltner and Sites[12] for samples with various types of Cu-based back contacts stored in both light and dark conditions with different electrical biases.

Table 2-3: Results of room temperature Hall measurements on CdTe:Cu crystals

Carrier concentration (10^{14} cm^{-3})	Resistivity (kΩ-cm)	Mobility (cm^2/Vs)	Condition
1.18	16.5	3.22	1 week after the 1st anneal.
5.3	13.5	0.9	Immediately after re-anneal.
0.7	21.4	4	1 week after re-anneal
6.4	12.3	0.8	2nd re-anneal
0.46	35.3	3.8	1 wk. after 2nd re-anneal
5.87	25.1	0.4	3rd re-anneal

From Table 2-3 it can also be noted that a drop in the carrier mobility accompanies each successive anneal. This drop in mobility could not be justified by an ionized impurity scattering mechanism; typically, an acceptor concentration of about 10^{18} cm^{-3} would be necessary to yield changes in mobility as the ones obtained in our experiment.[13] Instead, we propose an explanation based on a model developed by Seto.[14] In the Seto model, a large number of defect states is present at the grain boundaries of a polycrystalline material and act as traps for the free carriers. Upon capture of the mobile carriers, the traps become charged creating a potential energy barrier which impedes the motion of carriers across the grain boundaries. This model has been applied with good results by von Windhem and Cocivera[15] to explain carrier concentrations several orders of magnitude lower than the dopant concentration in CdTe samples. The dopants considered in their study included Cd, Te, Cu, Ag, In , O_2. A similar model, in qualitative agreement with Seto, was developed by Bennet.[16]

For our sample, we suggest that the grains are completely depleted and the grain boundary traps are only partly filled. After an anneal, some of the Cu acceptor states are restored leading to an increase in the acceptor concentration. This in turn leads to an increased number of carriers being trapped at the grain boundaries, therefore increasing the barrier height and reducing the mobility.

Using L=1μm for the average grain size and assuming that the dominant conduction mechanism at the grain boundaries is thermionic emission[17] we calculate that a change $\Delta N_A \cong 2x10^{14} cm^{-3}$ is necessary to explain the observed drop in the mobility. This value is in order-of-magnitude agreement with the observed change in the carrier concentration.

The decrease in carrier concentration of Cu-doped CdTe samples, suggested by PL and Hall experiments, should have important effects on the electrical characteristics of CdS/CdTe devices similarly doped.

To test this hypothesis, we used CdS(200nm)/CdTe(4000nm) devices grown on glass substrates by close-spaced sublimation. A 30 Å Cu layer was deposited on the free surface of the CdTe layer followed by a heat treatment as described previously. Note that a similar amount of Cu and anneal are typically used in the formation of a back contact to CdTe. To minimize effects due to a possible back-contact barrier the open-circuit voltage was measured using a high impedance electrometer. The current flowing through the CdS/CdTe device during measurement is estimated to be less than 0.1 pA. Based on the high absorption coefficient of the CdTe, we also assume that the radiation penetrating through the CdTe to reach the metal-semiconductor junction is negligible. From these considerations we believe that the measured V_{OC} is not significantly influenced by surface effects.

Changes in V_{OC} of the studied devices after stress under constant one-sun ($1000W/m^2$) illumination at 60 °C and subsequent re-anneals are illustrated in Figure 2-7. For comparison the V_{OC} of a sample without Cu processed in an identical way is also shown. The changes in the open-circuit voltage for the Cu-doped sample are consistent with the drop/recovery in the carrier concentration observed with Hall measurements. In contrast, the device without Cu shows a slight initial decay but appears largely insensitive to the effects of consecutive anneals. Also note that the undoped device shows a consistently lower open-circuit voltage relative to a Cu-doped device immediately after an anneal. This result is in agreement with Cu acting as a dopant of the entire CdTe layer as discussed in the previous chapter.

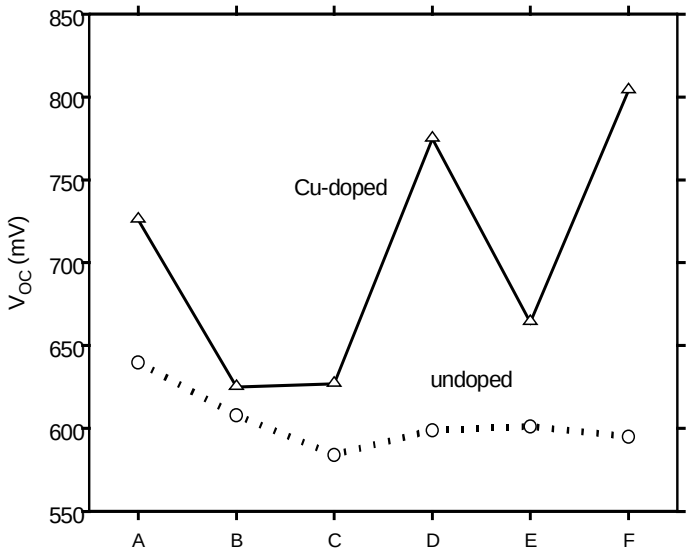

Fig. 2-7. Open circuit voltage variations of two CdS/CdTe cells with sequential light-soak stress and anneals. For one cell, the CdTe layer was deliberately Cu-doped, the other had no intentional Cu doping. Horizontal axis points are: A.- initial anneal; B-2days light soak (LS); C-35 days additional LS; D-second anneal; E-2 days LS; F-third anneal.

2.3.2 Photoluminescence in crystalline CdS doped with Cu

The PL spectrum of as-grown CdS excited with the 458 nm line of an Ar laser at an excitation density equivalent to two suns is shown in Figure 2-8. Note a broad bound excitonic peak at 2.546 eV, the I_2 line of Thomas and Hopfield,[18] and its phonon replica. This line has been identified as an exciton bound to a neutral donor. It is not surprising that this line dominates in as-grown CdS, which is known to be n-type. The lower-energy spectrum is dominated by a donor-acceptor-pair transition at 2.42 eV and its phonon replicas. The photoluminescence of nominally undoped as-grown CdS crystals has been extensively studied by other groups and will not be discussed further in this report.[18,19]

CdS:Cu samples were prepared by evaporating 20 nm of Cu on the CdS crystal, and annealing in flowing nitrogen at 385 C for 1 hour. As a control, a piece of CdS with no copper was annealed simultaneously under the same conditions. After annealing, luminescence from both the CdS and CdS:Cu samples is quenced by over two orders of magnitude and is barely detectable.

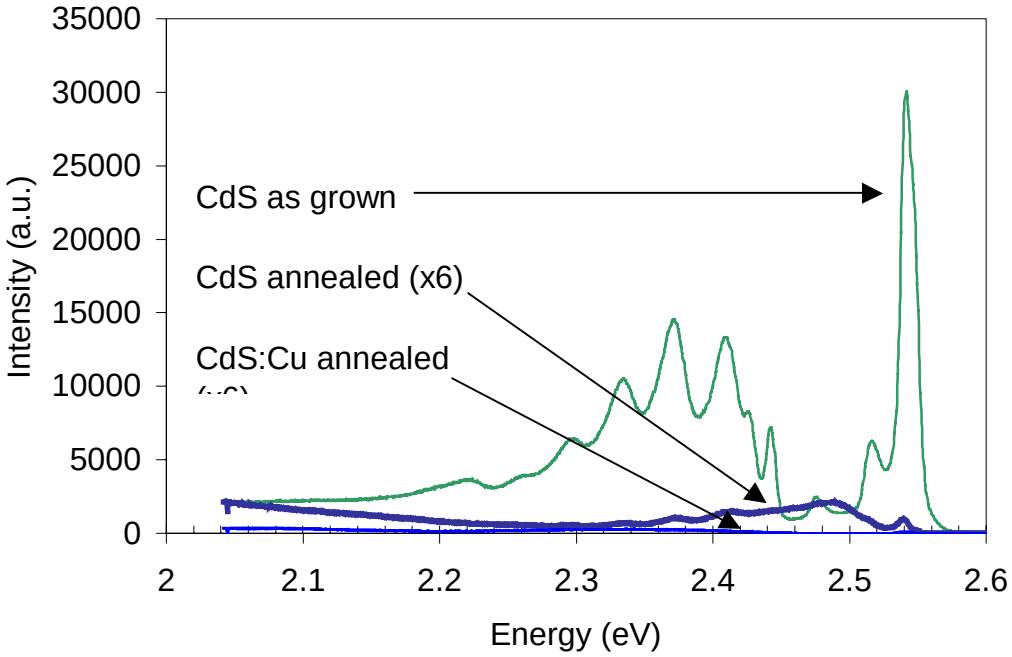

Figure 2-8 10K photoluminescence of single crystal CdS as grown, and annealed at 385 C with and without Cu. The excitation power density at 2.708 eV was equal to two suns.

At an excitation power density of 200 suns, the emission from all samples is dominated by exciton emission, shown in Figure 2-9. At this higher excitation power, the emission from the CdS and CdS:Cu annealed in N_2 is quenched as compared to the as-grown emission, though not to the extent that it is in the 2-sun spectra. In addition, one can see that the exciton peak from the CdS:Cu sample is at lower energy, approximately 2.542 eV, than the I_2 exciton that dominates the as-grown and annealed CdS spectra. The low intensity of the 2.542 eV emission raises the question of whether it appears only after the Cu-diffusion step, or whether it is actually present in the emission from the as-grown sample but is swamped by the dominant I_2 line. We cannot rule out the later possibility, but the fact that the 2.542 eV emision does not appear to be present in the annealed CdS sample seems to indicate that the 2.542 eV line results from an exciton bound to a Cu-related center.

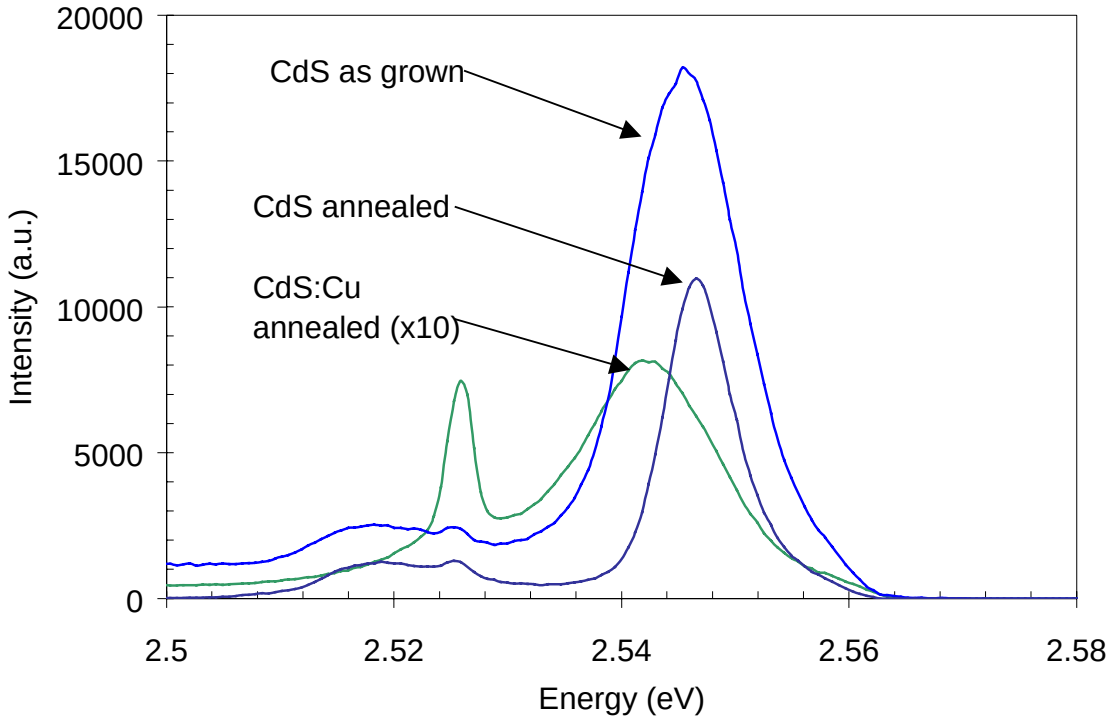

Figure 2-9 Exciton emission from CdS and CdS:Cu excited at 2.6 eV with 20 W/cm^2. The peak at 2.526 eV is a second order phonon-Raman peak. Note scale change for the CdS:Cu spectrum.

Low temperature photoluminescence was also examined in glass/ITO/CdS/CdTe devices without final contacts. Standard CdS/CdTe plates were obtained from First Solar. Part of each plate was coated with 10 nm of copper, then diffused at 200 C for 1 hour. Photoluminescence was performed using a 476.9 nm Ar laser line from the glass side in the regions with and without copper. Using a bare glass substrate, it was confirmed that no luminescence was detected from the glass. The PL signals at 10K are shown in Fig. 2-10.

The main effect of the Cu diffusion on the PL of the CdS layer is a quenching of the exciton-related emission. That this quenching occurs at all indicates that enough copper is reaching the CdS layer to affect electronic properties. The photoluminescence signal was observed to be stable over a period of several days in both the copper and no-copper regions. This is in contrast to the Cu-related photoluminescence in the CdTe layer near the junction of a CdS/CdTe device, as reported by Dan Grecu.

Thus in both single crystalline and polycrystalline CdS, it appears the main effect of 200 C copper diffusion on photoluminescence is a quenching of exciton photoluminescence. We have not seen evidence of any specific luminescence lines that can be unambiguously attributed to Cu-related states. We point out that in CdS, the levels of Cu in the Cu^+ and Cu^{2+} charge states are 1.20 eV and 0.73 eV respectively, energies that are not within the range of our present detector. We are currently constructing a photoluminescence system that is capable of detecting infrared luminescence.

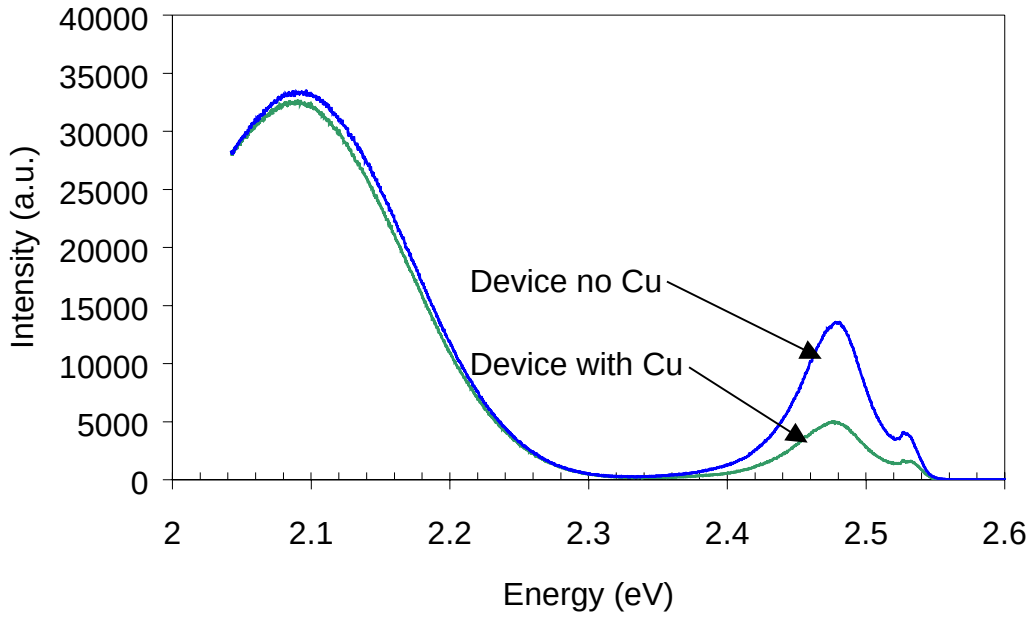

Figure 2-10 10K photoluminescence from the glass side of a CdS/CdTe solar cell underneath the copper contact ("with copper") and underneath a non-contacted region ("no copper"). Both regions were annealed at 200 C for 1 hour.

In both single crystal and polycrystalline CdS in a real device, we performed short-term shelf and light-soaking stability experiments. In both the device and the single crystal CdS:Cu, the PL is stable after storage in ambient conditions for five days, or after 2 days light soaking at one sun, in contrast to the case of CdTe:Cu. Longer term stability experiments have not been performed.

2.3.3 Effects of $CdCl_2$ treatment on PL from CdS single crystals.

The effects of $CdCl_2$ treatment on polycrystalline films have been studied extensively. This treatment is known to promote grain-growth and thought to passivate grain-boundary defects in polycrystalline CdS and CdTe, and is an essential post-growth processing step in the fabrication of CdS/CdTe solar cells. However, little is known about whether $CdCl_2$ treatment affects the *interior* of individual CdS or CdTe grains. To assist in answering this question, we have recently begun photoluminescence studies of the effects of $CdCl_2$ treatment on single-crystalline CdS and CdTe. In these studies the $CdCl_2$ treatment was performed by sealing the single crystal samples under vacuum in a glass tube containing $CdCl_2$ powder. The sealed tubes were then annealed at 387 C for 1 hour. This temperature and time are similar to the conditions used in the $CdCl_2$ processing of our polycrystalline devices, though in the latter case the treatment is done in our vapor-transport system in dry air. Thus there may be more oxygen or nitrogen present in the vapor-treatment process than in the tube-treatment process used in these preliminary studies. We chose to anneal with $CdCl_2$ in evacuated, sealed tubes for the initial study so that the effects of the $CdCl_2$ and those of air could be separated. Studies on samples treated using the vapor $CdCl_2$ process will be performed later.

In the case of CdS, annealing a single crystal with $CdCl_2$ reduces the photoluminescence emission intensity slightly with respect to the as-grown case, but the shape of the spectrum does

not change for 476.5 nm excitation. Similarly, PL from CdS:Cu annealed in $CdCl_2$ excited with 200 sun 476.5 nm light is identical to that of CdS:Cu annealed in N_2.

However, using the same excitation power density, but exciting with 752.5 nm (1.65 eV) light, one observes dramatically different PL behavior. Not surprisingly, as-grown CdS results in no detectable emission from 2.2 to 2.6 eV under 1.65 eV excitation. However, after annealing CdS or CdS:Cu in either N_2 or $CdCl_2$ at 385 C, we observe visible green luminescence, shown in Figure 2-11. Instead of exciton-dominated emission, we observe a donor-acceptor-pair transition

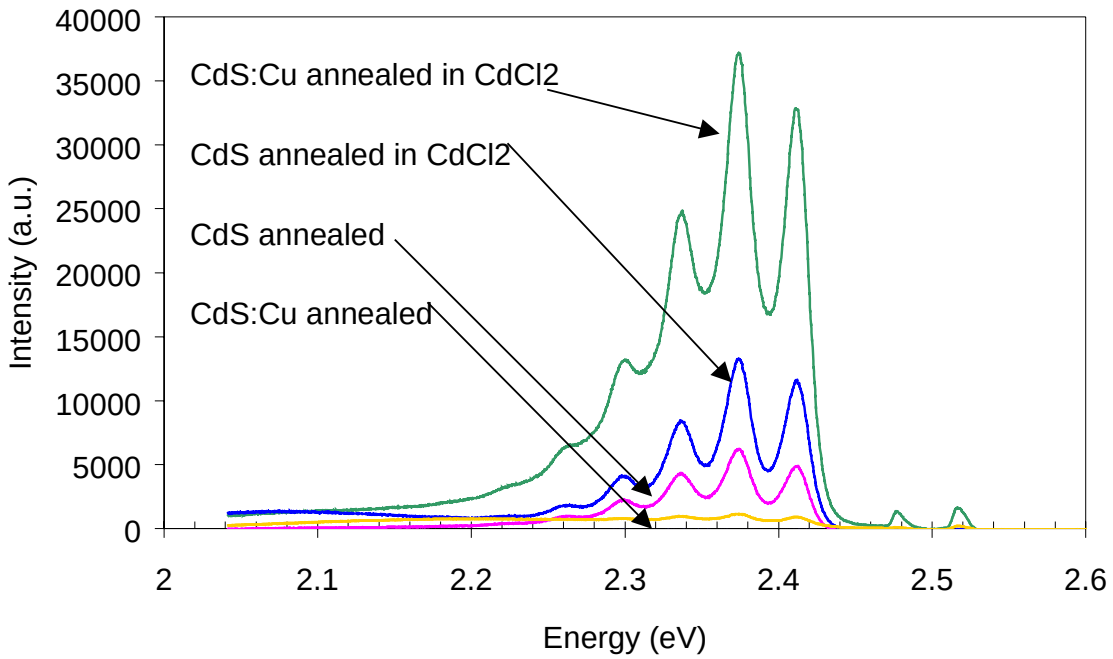

that is strongly coupled to the lattice, as evidenced by the many phonon side bands.
Figure 2-11. Green PL from CdS and CdS:Cu using deep red excitation at 752.5 nm (1.65 eV).

Clearly, this luminescence does not result from a valence-band electron being promoted directly to an emission center by a single photon since the emission energy is greater than the excitation energy. Instead, it is likely that the emission results from electrons excited from deep traps into the luminescent center.

Changes in the photoconductivity of CdS with the application of infrared light have been observed by several groups. This effect is attributed to the excitation of electrons from deep traps into near-band-edge states, and is thought to be related to Cd interstitials.[20] As is seen in Figure 2-11, the DAP emission in our samples is strongest in the samples annealed in $CdCl_2$, which is consistent with the involvement of a Cd interstitial site. One would expect strong lattice coupling to an interstitial center, just as is observed. Note that the presence of Cu also seems to enhance this emission, which may result when a Cu atom substitutes on a Cd site and the displaced Cd atom moves to an interstitial position.

The appearance of this emission after $CdCl_2$ annealing indicates that $CdCl_2$ treatment has an effect on the electronic states even on single-crystal CdS. To verify this, single crystals of CdS were annealed in $CdCl_2$ as described above, and the electrical resistivity was compared to that of one-mm thick, as-grown samples as calculated from current-voltage measurements with indium contacts. Measurements were taken in the dark and at one sun white light illumination.

Similar measurements were made on a one-micron thick, sputtered, polycrystalline CdS film before and after $CdCl_2$ annealing. The results are summarized in Table 2-4. In the case of the as-grown single crystal, the light resistivity is only slightly lower than the dark resistivity, indicating a relatively small number of electronic traps. After annealing in $CdCl_2$, the dark resistivity increases by four orders of magnitude, while the light resistivity increases by only an order of magnitude compared to the as-grown sample. This may be explained by an increased number of traps in the $CdCl_2$ annealed sample, increasing the dark resistivity, but also increasing the effect of light illumination on resistivity. Note that an increase in the number of deep states after $CdCl_2$ annealing is also consistent with the infra-red excited PL results above.

Table 2-4: Resistivity of CdS samples before and after annealing in $CdCl_2$

Sample	As-grown Crystal	$CdCl_2$ treated Crystal	As-grown Film	$CdCl_2$ treated film
Dark resistivity (Ωcm)	13.5	1×10^5	7.5×10^5	1.3×10^4
Light resistivity (Ωcm)	8	100	6.7×10^3	65
Dark/light ratio	1.7	1×10^3	112	200

The as-grown films have a much higher as-deposited resistivity, which is expected due to the large number of grain boundaries and defects present in a polycrystalline material. After annealing in $CdCl_2$ the resistivity of the film goes down, indicating grain growth and grain boundary passivation as has been seen in other studies. Note, though, that the dark/light resistivity ratio increases in after $CdCl_2$ annealing even in the thin film. This may be a result of an increased number of traps within the individual CdS grains. Previous studies on polycrystalline CdS films have established the importance of $CdCl_2$ treatment in enhancing grain growth and passivating grain boundaries.[21] Clearly in the case of polycrystalline films, effects of grain boundaries and grain boundary defects are of first order importance. However, the data shown here indicate that the effects of $CdCl_2$ on the interior of the grains may also be important.

Recently, Hegedus reported that red bias light affected the quantum efficiency of CdS/CdTe solar cell devices at wavelengths near the CdS band edge.[22] The effect was observed only for devices that had been subjected to certain stress conditions, and is not presently understood. We believe the states responsible for the 1.65 eV-excited green emission in CdS and CdS:Cu may be related to this effect, and are currently exploring this phenomenon further.

2.3.4 Effects of $CdCl_2$ on PL from CdTe crystals

We have done preliminary experiments to determine the effect of $CdCl_2$ annealing on CdTe single crystals. Single crystal CdTe chunks were provided by Alan Fahrenbruch. Small pieces were cut from the chunks and etched with bromine methanol solution to remove surface damage. Samples were prepared in sealed tubes as described above and annealed at 387 C for 1 hour. Results for PL excited at 20 suns of 752.5 nm light are shown in Figure 2-12. Note that the features of PL in as-grown CdTe are described in our 1998-1999 annual report.

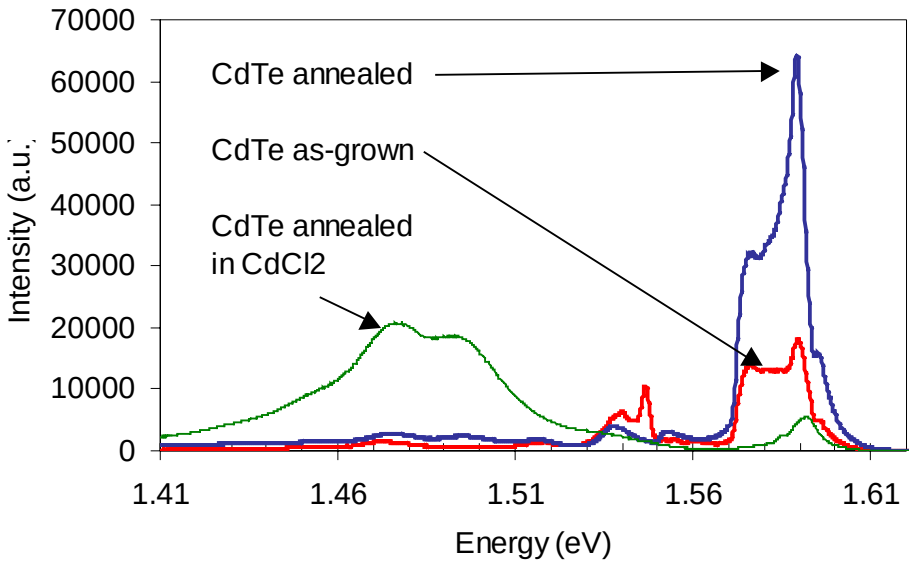

Figure 2-12: Photoluminescence from CdTe single crystals as-grown, annealed at 387 C, and annealed at 387 C in $CdCl_2$.

After annealing in an evacuated tube, the exciton luminescence increases by a factor of three and the feature at 1.55 eV associated with the Cd vacancy is somewhat smaller. There are few changes in the low-energy region of the spectrum. After annealing in the presence of $CdCl_2$, however, dramatic differences are observed. The exciton luminescence is quenched significantly, and the low-energy donor-acceptor pairs are dominant. This experiment shows that as in the case of CdS, the effect of $CdCl_2$ annealing has a strong effect on the intra-grain PL response of CdTe.

While the quality of the crystals used in this study is excellent, the large size and irregular shape of the chunks made reproducible sample preparation difficult. We are currently repeating this experiment using oriented, polished CdTe wafers from a commercial vendor.

2.3.5 Micro-PL of CdTe:Cu

In July of 1999 we began a collaboration with the research group of Gerardo Contreras at the National Polytechnic Institute (IPN) of Mexico City. This effort is supported jointly by the U.S. NSF International Programs Division and by Mexico's CONACyT science and technology support foundation. This effort is focused on studies of photoluminescence and electron spin resonance comparisons between large-grain, ~100 μm thick films grown at IPN by closed space sublimation (CSS), small grain, magnetron-sputtered (MS) films grown at UT, and single crystal CdTe 1 mm thick. We have studied PL spectra obtained from cleaved edges of both crystalline and polycrystalline samples to examine the diffusion from the surface inward, and to try to distinguish the effects of grain boundary diffusion. The 80K and 10K micro-PL capability of the Mexico City group is facilitating this effort. We find that the data are very sensitive to laser excitation power density and post deposition/growth treatments in $CdCl_2$, Cd, or Te overpressures. UT is continuing macro-PL and IPN is studying micro-PL of single-crystal and polycrystalline CdTe and CdS, with and without copper doping.

2.4 Absorption and PL measurements on S-rich CdSTe alloy films at 10K

In our Phase 1 annual report we presented absorption spectra at 10 K for pure CdTe films, for the Te-rich alloy, $CdS_{0.04}Te_{0.96}$, for pure CdS, and the S-rich alloy, $CdS_{0.95}Te_{0.05}$. The Te-rich films showed well-defined excitonic features after $CdCl_2$ treatment but not the S-rich films. The S-rich alloy (x = 95%) showed considerable below-band-edge absorption both before and after $CdCl_2$ treatment. In order to explore further these tail states in S-rich films, which may be important in limiting the minority carrier lifetime in lightly Te-alloyed CdS, Diana Shvydka prepared, by pulsed laser deposition, a set of films with extremely low alloying, approximately 0.3% Te, 1% Te and 5% Te. Film compositions were determined by wavelength dispersive x-ray spectroscopy (WDS) characterization at NREL by Amy Swartzlander-Guest.

The effect of slight alloying on the band tail absorption in the S-rich films is shown in Fig. 2-13. Note that there is a substantial red shift of the band edge with Te concentration, but also that band tail absorption, 0.5 eV or more below the band edge, increases with Te concentration. After annealing with the standard vapor $CdCl_2$ treatment, the position of the absorption edges shifts slightly higher and the absorption tails decrease slightly as seen in Fig. 2-14.

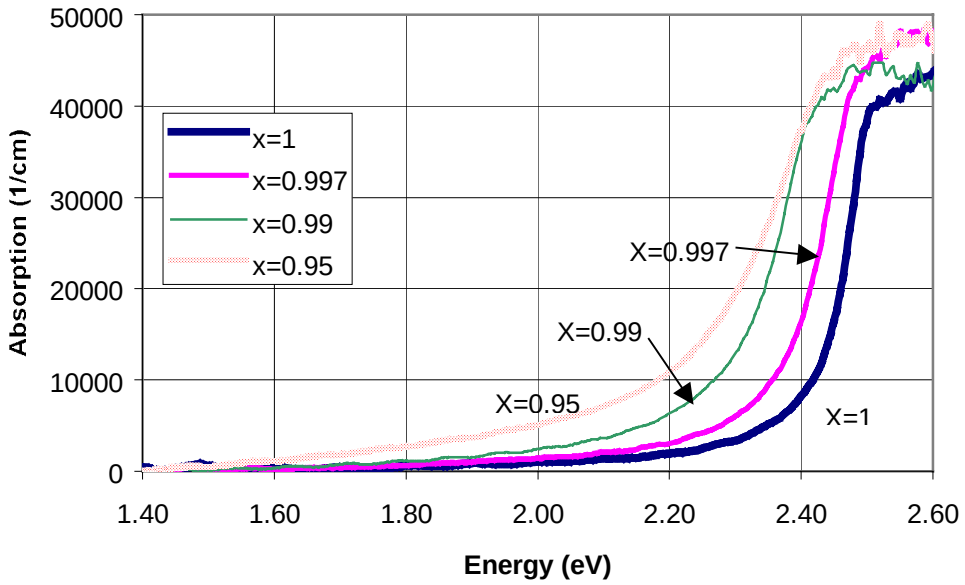

Figure 2-13. Absorption coefficient of as grown CdS-rich alloy films near the fundamental absorption edge, measured at 10 K.

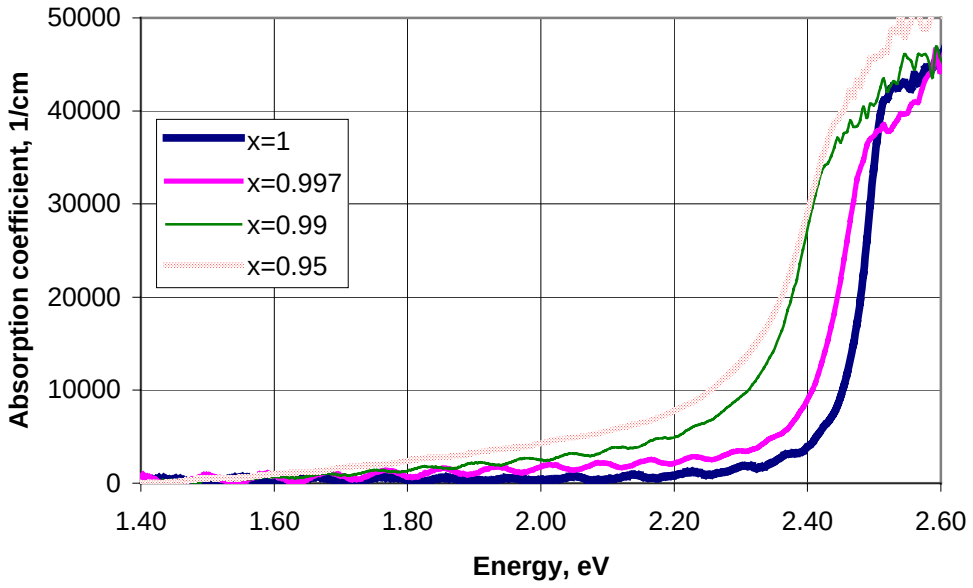

Fig. 2-14. Absorption of CdS-rich films after vapor $CdCl_2$ treatment, measured at 10 K.

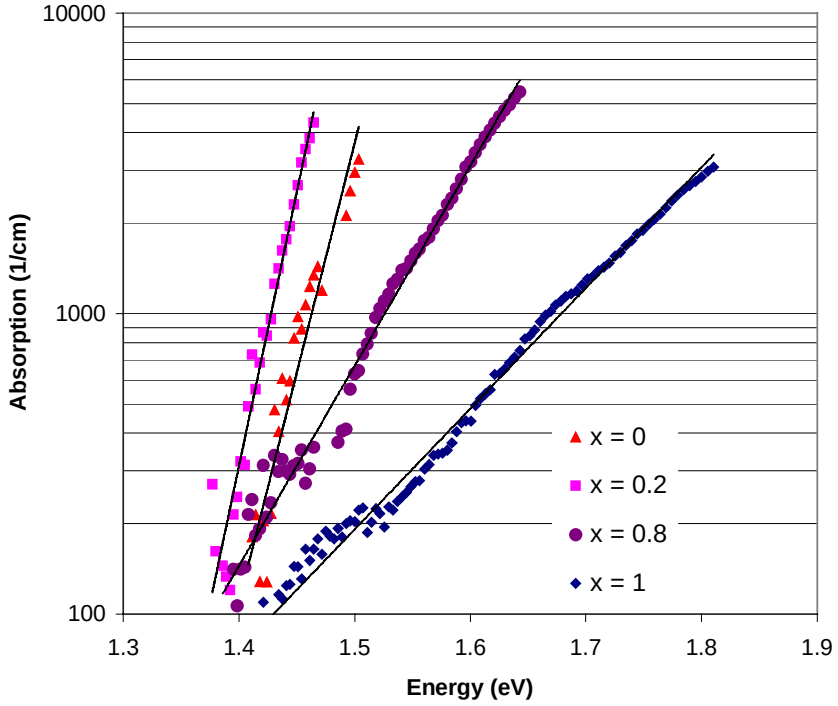

Figure 2-15. Absorption coefficients for pulsed laser deposited (PLD) films of different concentrations measured at room temperature

To examine the nature of the sub-band-gap absorption in these alloys we show in Figure 2-15 on a logarithmic scale the experimental absorption coefficients for untreated films prepared by pulsed laser deposition. In this figure, we focus on the region of moderate absorption in which the absorption coefficient ranges from 10^2 to 4 x 10^3 cm^{-1}. There is some residual oscillation due to incompletely corrected interference effects, but the absorption coefficient clearly depends exponentially on photon energy just below the band edge. The strong band bowing of the alloy CdS_xTe_{1-x} is clearly shown in this figure by the fact that the absorption for x-0.2 lies to the red (lower energy) side of that for x=0.

The exponential behavior of the absorption coefficient, α, near the fundamental absorption edge qualitatively agrees with the Urbach rule:[30,31]

$$\alpha = \alpha_0 \exp\left[S\left(E - E_0\right)\right], \tag{2-1}$$

where α_0 and E_0 (the band gap) are dependent on the alloy composition and S is a slope parameter. In the case of single crystal, non-alloyed materials, the temperature dependence of the slope parameter often can be written as:

$$S = S_0 \frac{1}{\hbar\omega_0} \tanh\left[\frac{\hbar\omega_0}{2kT}\right], \tag{2-2}$$

where $\hbar\omega_0$ is the energy of the LO phonon in the crystal. One component of the Urbach tail is that the phonon produces a modulation of the band gap which is temperature dependent because the phonon mean square amplitude depends on the phonon occupation number. However, in the case of the CdS_xTe_{1-x} alloy system the CdS-like longitudinal optical (LO_2) phonon energy changes relatively little with composition and the CdTe-like mode (LO_1) changes hardly at all, as shown by Table 2-5. (Data are from Ref. 23.)

Table 2-5. LO phonon energies and Urbach slope parameters for CdSTe

Sample x (%)	Phonon energies, hw_0 (meV)		Slope parameter, 1/S (meV) (from exponential fit)
	LO_1	LO_2	
0	21.6		28.4
0.2	21.3	33.7	23.8
0.8	20.7	36.2	65.4
1		37.7	107.5

In contrast with the predictions of Eq. 2-2 above, our data from room temperature and 10K clearly show very little temperature dependence as would be expected from phonon mediated band edge tailing. Rather, it seems quite clear that alloy potential fluctuations dominate the Urbach tail in these alloy films. One evidence of this is that the film with x=0.2 has the steepest slope (smallest 1/S). This composition happens to be very near the minimum in the band bowing so that fluctuations in the local alloy composition would have little influence on the band edge.

2.5 Quantum efficiency of rf-sputtered cells vs. CdTe thickness

In our last Annual Report, we provided data on cell efficiencies as a function of CdTe thickness down to about 0.5 μm. Results on the open circuit voltage, short circuit current and fill factor were reported on one set of cells. Ilvydas Matulionis and Jennifer Drayton have completed additional cells and measurements in the present Phase. As reported last year, the V_{OC} stays at or above 800 mV for CdTe thickness as low as 1.3 μm; the J_{SC} shows little drop in the best cells down to 1.3 μm also. However, there is a noticeable drop in the fill factor. Nevertheless, we have fabricated cells with only 1.3 μm of CdTe having efficiencies of over 10% (or within about 1.5% absolute of our best rf sputtered cells). But for the two sets of cells fabricated with thinner CdTe (0.73 and 0.47 μm) the best cell efficiencies were only 8.5% and 3.3% respectively.

The quantum efficiencies as a function of CdTe thickness are shown in Fig. 2-16. These data show most importantly that the collection suffers all across the spectrum, particularly in cells with CdTe thickness below 1.0 μm. Presumably in the cells with thin CdTe, the junction parameters have degraded.

Although cell performance appears to hold well at least for CdTe thickness down to almost 1 μm, the durability and stability of these thin CdTe devices will need to be proved. The dependence of cell performance with thin CdTe is now being checked with a new set of cells. The general behavior appears to be reproducible but data from a new set of samples show that it is possible to maintain higher efficiency and QE responses (than given in Fig. 2-16) over the range from 0.5 to 3.0 μm. A more detailed study will be reported in the next Annual Report.

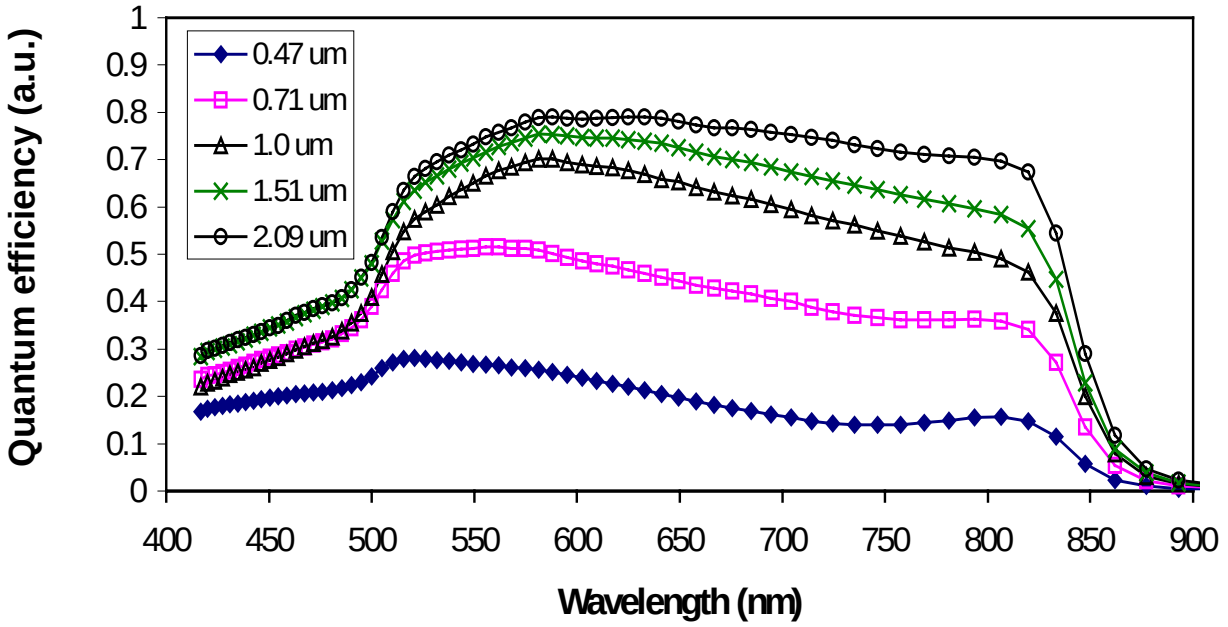

Fig. 2-16 Quantum efficiencies of four rf sputtered cells with different thicknesses of CdTe.

2.6 Preliminary studies of substrate CdTe cells

During the past year we have begun some studies of CdS/CdTe cells grown by magnetron sputtering in the substrate configuration. We believe that successful growth in this configuration can lead to improved understanding of the CdS/CdTe interface and more flexibility in trying other heterojunction partners to p-CdTe. The substrate configuration obviates the need for a transparent superstrate, e.g., glass, and might facilitate fabrication on thin, flexible substrates with their advantages in large-scale fabrication and in application. In addition, it is likely that this configuration will be needed in the development of tandem junction cells in which the CdTe absorber layer (or wider-band-gap II-VI alloy) lies above a bottom cell of Si, or CIS, or perhaps HgCdTe.

In this work, Ilvydas Matulionis began with the use of 125 μm stainless steel foil similar to that used for a-Si:H-based cells by Prof. Deng's group. These cells exhibited very poor PV response and had problems with adhesion during the $CdCl_2$ treatment step. More promising results were obtained with the use of 100 μm molybdenum sheet for substrate material. Three cell configurations gave promising results. These are, in order of increasing performance:

Mo/CdTe/CdS/ITO;
Mo/Cu/CdTe/CdS/ITO and
Mo/ZnTe/CdTe/CdS/ITO.

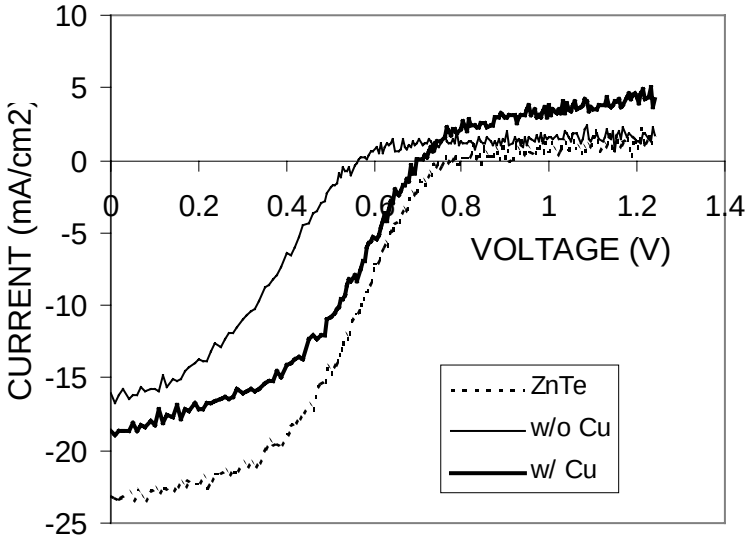

Fig. 2-17. I-V behavior of superstrate cells sputtered on Mo substrates

For the CdTe grown without the ZnTe intefacial layer on Mo, we also tried using a 2 nm layer of evaporated Cu before the CdTe. The CdTe and CdS were grown at 360 C and a $CdCl_2$ treatment at 387 C was performed after the CdS deposition. The ITO top contact was deposited under rf sputtering conditions similar to those used for a-Si:H top contacts. The results below were obtained from small 0.045 cm^2 dots obtained by masking during the ITO sputtering. As the I-V curves of Fig. 2-17 show, there appears to be a strong back-diode effect which blocks current in the forward direction. This occurs for all three Mo-CdTe interface structures. This certainly indicates an area for future studies. Nevertheless, we are encouraged by the fact that efficiencies approaching 8% were possible in these initial efforts, well above those reported by Singh, et al.[24]

2.7 Development of sputter target pressing capability

In the first year of this effort, we successfully used cold pressing to fabricate thin, two-inch sputter targets in-house. However, these targets often deteriorated after two or three deposition runs. Therefore, during Phase II we fabricated a die and press which we can use with our existing hydraulic press to fabricate thicker sputter targets at temperatures up to 400 C. This now allows us to fabricate special allow compositions for exploratory work. We plan to use this to fabricate mixed CdS/CdTe and CdTe/ZnTe targets for sputter deposition of these alloys.

2.8 Development of variable temperature I-V system

Each summer for the past several years, students from the NSF-sponsored Research Experiences for Undergraduates program (see below) have participated in our group. For Summer 1999 one of the students was Adam Smith from Michigan State University. As his project, he constructed a Peltier-cooled stage for making temperature-dependent I-V measurements on solar cells. He collaborated with graduate student Konstantin Makhratchev in this project and adapted a computer power supply for the Peltier driver. The sample is mounted on a copper stage containing a small hole used for illumination. Cooling to several temperatures between room temperature and –24C was easily achieved with the Peltier heat pump system. The sample temperature was monitored with a nickel-iron thermistor. Figure 2-18 shows data from one of Adam's first measurements. Although this particular cell had much less than optimum performance, the data demonstrate the system operation.

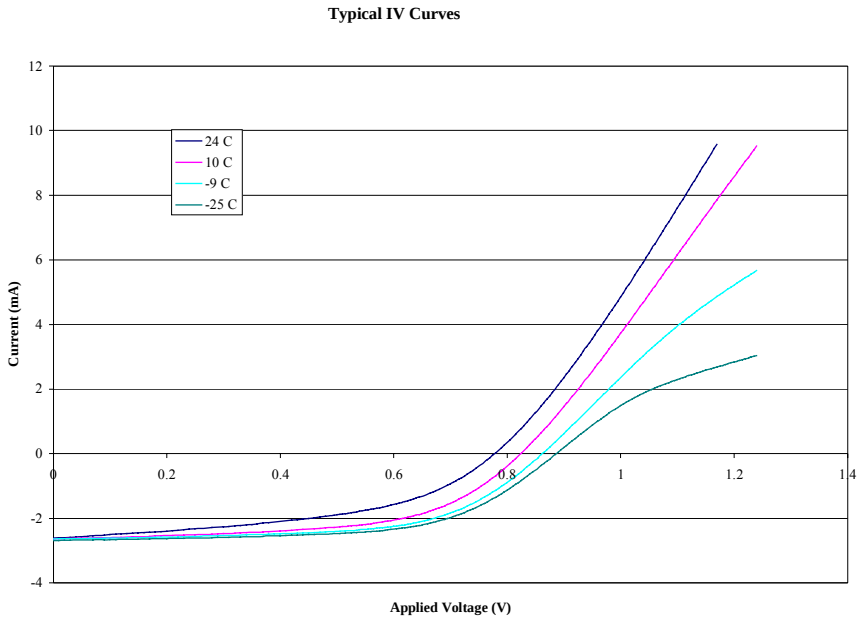

Figure 2-18 I-V curves at various temperatures for Cu/Au contacted solar cell.

Temperature-dependent I-V measurements provide an important diagnostic for examining non-ohmic behavior associated with, e.g., back contacts. Brian McCandless, *et al*,[25] have shown

that one can use temperature-dependent I-V measurements to estimate interface barrier heights in CdTe/CdS solar cells.

In this project Adam calculated the slope R of the I-V curve at forward bias, and assumed that the non-zero slope, or "roll-over" in this region is due to the blocking behavior of a reverse diode. The barrier height is then given by the slope of the Arrhenius plot of ln(R) vs. q/kT. Initial measurements on UT-fabricated solar cells with standard Cu/Au contacts indicate a barrier height of ~0.2 eV, in reasonable agreement with the IEC value of 0.3 eV for their cells.[25] This work is now continuing with comparison studies of cells with Cu/Au contacts and those with ZnTe-based contacts free of copper.

2.9 Teaming activity

2.9.1 Hall measurements on HRTs

In our last annual report, we provided results of Hall measurements on a variety of tin-oxide films including the standard LOF material, Golden Photon HRT material, and three types of high resistivity material provided by Peter Meyers of ITN Energy Systems. Randy Bohn has recently extended the temperature range of these measurements and, in some cases, has been able to obtain separately the activation energies for the mobility and carrier concentration. Some of the additional results are described below and provide some insight into the different role of Cd and Zn dopants in the SnO_2.

Hall measurements were made on a sample of high resistivity tin oxide on borosilicate glass from Golden Photon with a thickness of 0.78 micrometers (measured by absorption and profilometry). Measurements were made in the dark and under AM1.5 (ELH lamp) conditions at temperatures from 290K to 360K. The material has a room temperature resistivity of 84 Ω-cm after several days in the dark. The corresponding room temperature light resistivity is about 43 Ω-cm, although there was no attempt to wait for this to reach equilibrium under these light conditions. (There was a slow drift toward lower resistivity values with time.) Hall measurements are marginal on these low mobility samples, but we estimate that the carrier density in the dark is around 3.7×10^{17} /cm^3 and that the mobility is of the order of 0.2 cm^2/V-s. The majority of the Hall measurements indicated negative charge carriers and this was verified using a hot probe method. However, it should be noted that there may be some uncertainty here because of the sample size. Finally, the activation energy from 290K to 360K for the dark conductivity is around 0.090 eV. In the light this decreases to about 0.034 eV. Note that here the sample was left in the dark at room temperature for 72 hours heated in the dark to 360K and then cooled and illuminated under AM1.5 conditions to room temperature. The data are shown in Fig. 2-19.

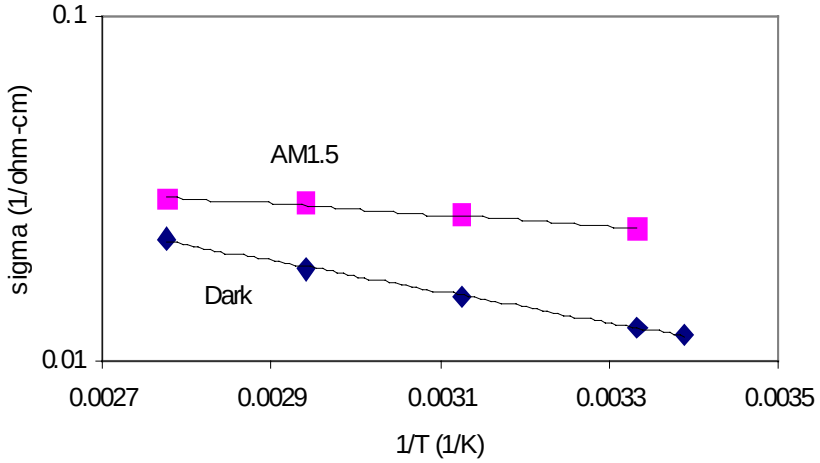

Figure 2-19: Conductivity vs. 1/T for GPI HRT material. The straight line fits yield activation energies of 0.090 and 0.034 eV for dark and light, respectively.

2.9.2 Sputtered cells on bilayer ITO from IEC

We have sputter deposited CdS/CdTe cells on ITO bilayer-coated glass obtained from Brian McCandless at IEC. The 200 nm of conductive ITO (15 Ω/sq, ρ=0.0003 Ω-cm) was covered with a 100 nm of resistive ITO (4000 Ω/sq, ρ=0.04 Ω-cm) to test the suitability of this material for improved open circuit voltage and efficiency of cells prepared with thinner CdS than our standard 0.13 μm. We prepared several cells on substrates with this ITO bilayer (on both borosilicate glass and 1-mm soda lime glass) and compared these with cells fabricated on 8 Ω/sq LOF glass in side-by-side depositions.

For cells with as-deposited CdS layers of 130 nm, we found only marginally higher efficiencies in the cells with the ITO bilayers (11.5% to 12%) compared with our standard cells on LOF SnO_2 (11 to 11.5%). For cells with as-deposited CdS layers of 40 nm, the J_{SC} was increased by 2.4 mA/cm^2 for both ITO-coated substrates and LOF-SnO_2 substrates. In both cases there was considerable loss of V_{OC}, although somewhat less severe in the bilayer ITO. V_{OC} dropped from 810 mV to 616 mV on the bilayer ITO and from 810 mV to 570 mV on the LOF-coated substrates, which had no HRT. We conclude that this bilayer ITO, while effecting some marginal improvement in cell performance (9.7% vs. 8.7% for standard LOF substrates) with the 40 nm of CdS, does not meet the needs of an HRT compatible with the rf sputtering process for CdS and CdTe. It has been suggested that an appropriate interfacial, high resistivity layer for the SnO_2/CdS interface might need to be in the range of 100 to 1000 Ω-cm. If so, the 0.04 Ω-cm HRT layer of this ITO bilayer would be considerable too conductive.

2.10 Collaborative Activity

2.10.1 Synchrotron EXAFS and GIXRF studies

In other work, we have prepared samples for Yi Han Kao and his group at the National Synchrotron Light Source in Brookhaven. They have measured depth profiles with grazing incidence x-ray reflection. In addition, they have recently obtained the first results on lattice location of Cu in CdTe by means of extended x-ray absorption fine structure (EXAFS). The following discussion is excerpted from the Applied Physics Letter recently published.[24]

In this study we diffused Cu into single crystal CdTe by evaporating 10 nm of Cu at room temperature and then diffusing for 1 hr at 200 C in air. The remaining metallic and oxidized Cu on the surface was removed by a 15 sec dip in 0.5% Br in methanol. The group of Y.H. Kao performed angular dependence of x-ray fluorescence (ADXRF) and x-ray absorption fine structure (XAFS) measurements at beamline X3B1 of the NSLS at Brookhaven National Lab. The Cu K-edge XAFS experiments were performed before and after a second 200 C heat treatment at Brookhaven. A conventional x-ray fluorescence detection mode was adopted to obtain the XAFS data. The detailed experimental procedure was same as described in previous experiments.[27] The quantitative information of the local structures around Cu in the sample before and after the secondary heating was obtained by a curve-fitting method using the backscattering amplitude and phase-shift functions extracted from theoretical models calculated from a well-known FEFF program.[27,28] The local structural parameters determined by this curve-fitting procedure are listed in Table I. From the detailed curve-fitting, the first and second prominent peaks in the Fourier-transforms have been identified as arising from Te neighbors around the Cu impurities in CdTe. Before secondary heating, the first Te neighboring shell has a coordination number of 4.1 at a distance of 1.68Å and the second Te neighbors are at 2.61Å from

Cu with a coordination number 2.7. As compared to the Cd-Te bond length of 2.81Å in bulk CdTe, the short distance 1.68Å between Cu and the first Te neighboring shell shows that some Cu atoms do not substitute for the cation Cd sites in CdTe. A plausible suggestion for the location of these Cu impurities is the formation of some small Cu-Te complexes around the Te atoms in the host CdTe, possibly accompanied by some local distortion of the CdTe unit cell. Since no other Cu near neighbors are found, it suggests that the Cu impurities do not form clusters by themselves. In addition, the EXAFS spectra have been compared with those obtained from a Cu_2Te compound, and our EXAFS data do not indicate the presence of detectable amounts of Cu_2Te in the material either before or after the second heating.

The second peak in the Fourier transformed EXAFS spectra of Cu indicates a near neighbor shell at 2.61Å, this is most likely due to Cu which are substituted on Cd sites but associated with a rather large local lattice distortion. Although this Cu-Te bond is shorter than the original Cd-Te bond in the host, by considering the experimental uncertainties and the fact that the ionic radius of Cu is about 0.13 Å shorter than that of Cd in a tetrahedral bonding configuration, a decrease of bond length from 2.81Å to 2.61Å seems reasonable. In fact this change in bond length is also consistent with a recent calculation by Wei, et al,[28] in which they predicted the Cu-Te bond length to be about 6.7% shorter than the CdTe bond. This translates to 2.62 Å for the Cu-Te bond in CdTe:Cu, the same as indicated by these EXAFS data.

After the second heating, the coordination number of the first Te neighboring shell was reduced to 2.3 with an increased local disorder as indicated by an increase of the Debye–Waller factor σ^2 (see Table I), but the bond length remains unchanged at 1.68 Å. The coordination number of the second Te neighbors was reduced to 1.7 with a slight increase of the bond length to 2.65 Å. This result suggests that heating at a moderate temperature of ~200 °C has not caused any substantial changes in the location of Cu impurities except for a reduced effective coordination number of Te atoms around Cu, mainly caused by the presence of additional local disorder associated with a broader redistribution of the Cu impurities. The second Fourier transform peak only shows a decrease of coordination number from 2.3 to 1.7 while the bond length and local disorder seem to remain practically the same within our experimental uncertainties. This might suggest that heating could lead to a possible reduction of the substitutional Cu impurities as a result of a broader and deeper distribution of all the Cu atoms. Hence, the main effects of heating could be attributed to a decrease of the coordination numbers and/or an increase of local disorder while the Cu impurities are redistributed through a deeper and broader depth profile in the CdTe host.

Additional samples are being prepared for further synchrotron x-ray studies in collaboration with Dave Albin to try to obtain better numbers and to try to follow with EXAFS the instability of Cu-related sites which were observed by Dan Grecu in PL.

Table 2-6. Parameters of local structure around Cu atoms obtained from curve-fitting the Cu K-edge EXAFS. The amplitude reduction factor S_0^2 representing the central atom shake-up and shake-off effects and the mean free path of photoelectrons λ are determined from curve-fitting the data of a pure Cu sample with coordination numbers and interatomic distances obtained from x-ray diffraction data[a]. N is the coordination number. R is the bond length. σ^2 is the Debye-Waller-like factor serving as a measure of local disorder. ΔE_0 is the difference between the zero kinetic energy value of the sample and that of the theoretical model used in FEFF.[23]

Sample	Atom	N	R (Å)	σ^2 (10^{-3} Å^2)	ΔE_0 (eV)	λ (Å)	S_0^2
CdTe	Te	4.1	1.68	14	0.7	6.1	0.8
	Te	2.7	2.61	11	0.9	6.1	0.8
CdTe heated	Te	2.3	1.68	23	-1.0	6.1	0.8
	Te	1.7	2.65	10	4.5	6.1	0.8

2.10.2 Laser scribing

We have continued some effort on laser scribing during Phase 2. Ilvydas Matulionis, with Dr. Compaan provided assistance to Dr. Noufi's group at NREL in reconditioning a frequency-doubled Nd:YAG laser scribing system. In addition, we have assisted Alan Delahoy of EPV in evaluating issues related to scribing of CIGS-based materials by executing a variety of scribes in materials supplied by EPV.

2.10.3 DOE Basic Research Opportunities in Photovoltaics (BROP) Workshop

On May 3, 1999, ADC participated in the BROP workshop organized by Bob McConnell, Satyen Deb, and John Benner. This was a follow-up to an earlier workshop organized by Alex Zunger in July, 1992. The CdTe workgroup consisted of J.R. Sites, R.W. Birkmire, C.S. Ferekides, A.L. Fahrenbruch and A.D. Compaan. The review paper is published as part of the *Electrochemical Society Proceedings*, vol. 99-11. The manuscript is: "Critical Issues and Research Needs for CdTe-Based Solar Cells," by A.D. Compaan, J.R. Sites, R.W. Birkmire, C.S. Ferekides, and A.L. Fahrenbruch.

2.11 NSF-REU/RET student participation

As in previous years, we have been privileged to be able to involve outstanding undergraduate physics students in our PV research through the support of the National Science Foundation. In the summer of 1999, two students joined the UT PV group. Catherine Taylor from Westminster College worked with Xunming Deng on a-Si:H –related problems and Adam Smith from Michigan State working with Al Compaan on CdTe-related problems. In addition, this year for the first time, the NSF program has been expanded to include Research Experiences for Teachers. David Simmons, who teaches physics at St. John's Jesuit High School in Toledo, worked on stress testing of CdTe cells.

2.12 Conclusions/Future Directions/Acknowledgments

Significant effort during the past year has been placed on improving the quality and reproducibility of the ZnTe:N interfacial layer for CdTe back contacts. We have been able reliably to obtain p-type doping levels of 5×10^{18} cm^3 in the rf sputtered ZnTe. However, contact resistance is not so reproducible and this appears to be related to properties of the CdTe surface layer. We believe that some of this variability may be due to unintentional, residual copper in the CdTe, some of which may come from the $CdCl_2$ treatment. In the coming year, we shall focus on achieving some doping of the CdTe near the back contact. The objective is to achieve a high quality, reproducible, stable, and manufacturable back contact to polycrystalline CdTe. Since the nitrogen-doped ZnTe has excellent transparency, it could be very useful as part of a "tunnel junction" in a tandem PV structure with a lower band-gap film underneath.

We have continued to identify the role of Cu in both CdTe and CdS, primarily through photoluminescence but also with Hall measurements, EXAFS (through collaboration with Yi Han Kao and his group at the NSLS at Brookhaven), cell performance changes, and other techniques. We will continue to maintain focus on improved understanding of factors which affect stability including the role of copper in CdTe and CdS as well as interdiffusion at the CdS/CdTe interface.

Optical studies of the CdSTe alloy system, using PL and absorption will emphasize the changes in properties of the almost pure binaries, CdTe and CdS, with trace amounts of S or Te, respectively. Our capability for laser scribing with excimer and Nd:YAG laser systems has been utilized by collaborators and continues to be available to the thin-film PV community. We shall continue full participation in the National CdTe PV Team and continue our involvement with several other outside collaborators.

Many individuals, in addition to those at the University of Toledo, listed under Project Personnel, have contributed substantially to our success in the past year. This includes Dan Grecu, Gary Dorer, Upali Jayamaha, Doug Rose, and others at First Solar, LLC. The members of the National CdTe PV team have been important in one or more projects reported here—from exchange of samples to illuminating discussions. We especially thank LOF for a supply of superstrate material and Brian McCandless (IEC) for other superstrates with ITO/HRT bilayers. We are especially grateful to NREL for support and to Bolko von Roedern, our contract monitor for his support and advice.

2.13 References

1. R.W.B. Pearse and A.G. Gaydon, *The Identification of Molecular Spectra*, Chapman and Hall, London, third edition (1965).
2. K. Kimura, *et al*., Journal of Crystal Growth 184/185, p. 411, 1998.
3. D. Grecu, Ph.D. Thesis, University of Toledo, unpublished 1999.
4. D. Grecu, and A.D. Compaan, "Photoluminescence Study of Cu Diffusion in CdTe," *NCPV Photovoltaics Program Review*, edited by M. Al-Jassim, J.P. Thornton, and J.M. Gee, AIP Conf. Proc. #CP462 (1999)
5. D. Grecu, and A.D. Compaan, "Photoluminescence study of Cu diffusion and electromigration in CdTe," Appl. Phys. Lett. **75**, 361 (1999).
6. D. Grecu, A.D. Compaan, D. Young, U. Jayamaha, & D.H. Rose, J. Appl. Phys. **88**, 2490 (2000).
7. E. Kucys, J. Jerhot, K. Bertulis, V. Barris, Phys. Stat. Sol. **59**, 91 (1980)
8. B. Yang, Y. Ishikawa, T. Miki, Y. Doumae, M. Isshiki, J. Cryst. Growth.**179**, 410 (1997).
9. M. Rub, N. Achtziger, J. Meyer, U. Resilohner, P. Rudolph, M. Wienecke, W. Witthuhn, J. Cryst. Growth **138**, 285 (1994).
10. J. Tang, PhD Thesis, Colorado School of Mines, 1998
11. E. Bykov, Masters Thesis, University of Toledo, 1997
12. J. Hiltner, J.R. Sites, *Proc. of the 15th NCPV Photovoltaics Program Review Meeting* (eds. M. Al-Jassim, J.P. Thornton, and J.M. Gee, AIP CP **462**, 1998) p. 170.
13. (see for example) P.Y. Yu, M. Cardona, *Fundamental of Semiconductors*, Springer-Verlag, Berlin Heidelberg, 1996, p.210.
14. J. Y. W. Seto, J. Appl. Phys., **58**, 3470 (1985)
15. J.A. von Windheim and M. Cocivera, J. Phys. Chem. Solids **53**, 1 (1992).
16. M.S. Bennet, J. Appl. Phys., **58**, 3470 (1985).
17. (see for example) M. Shur, *Physics of Semiconductor Devices,* Prentice Hall, Englewood Cliffs, New Jersey, 1990, p. 204.
18. D. G. Thomas and J. J. Hopfield, Physical Review **128**, 2135 (1962)
19. N. S. Bogdanyuk, G. E. Davidyuk, and A. P. Shavarova, Semiconductors **29**, 99 (1995)
20. A. Mandelis and E. K. M. Siu, Physical Review B, **34**, p. 7209 (1986)
21. W. Song, D. Mao, J.U. Trefny, R. K. Ahrenkiel, D. H. Levi, and S. Johnston, *15th NCPV Photovoltaics Program Review*, p. 188 (1999)
22. S. Hegedus, presentation at National CdTe Team Meeting, Golden, CO, January, 2000 (unpublished)
23. A. Fischer, Z.Feng, E.Bykov, G.Contreras-Puente, A.Compaan, "Optical phonons in laser-deposited CdS_xTe_{1-x} films," Appl. Phys. Lett. **70**, 3239, 1997
24. V.P. Singh, J.C. McClure, G.B. Lush, W. Wang, X. Wang, G.W. Thompson, and E. Clark, Solar Energy Materials and Solar Cells, **59**, 145-161 (1999); see also, D.K. Schroder, *Semiconductor Material and Device Characterization*, (Wiley, New York, 1990) pp. 130ff.
25. B.E. McCandless, J.E. Phillips, and J. Titus, 2nd World Conference and Exhibition on Photovoltaic Solar Energy Conversion, 6-10 July, 1998, p. 448.
26. Y.L. Soo, S. Huang, S. Kim, G. Kioseoglou, Y.H. Kao, A.D. Compaan, D. Grecu, and D. Albin, "Effects of heat treatment on diffusion of Cu atoms into CdTe single crystals," Appl. Phys. Lett. **76**, 3729 (2000).

27. Y. L. Soo, Z. H. Ming, S. W. Huang, Y. H. Kao, R. N. Bhargava, and D. Gallagher, Phys. Rev. B **50**, 7602 (1994), and references cited therein.
28. J. J. Rehr, J. Mustre de Leon, S. I. Zabinsky and R. C. Albers, J. Am. Chem. Soc. **113**, 5135 (1991).
29. S.H. Wei, S.B. Zhang, A. Zunger, J. Appl. Phys. **87**, 1304 (2000).
30. F. Urbach, Phys. Rev. **92**, 1324 (1953).
31. L. Samuel, Y. Brada, A. Burger, and M. Roth, Phys. Rev. B **36**, 1168 (1987); L. Samuel, Y. Brada, and R. Beserman, Phys. Rev. B **37**, 4671 (1988).

3 Amorphous Silicon Based Cells and Materials

3.1 Comparison Study of a-SiGe Solar Cells and Materials Deposited Using Different Hydrogen Dilution

3.1.1 Summary

A-SiGe n-i-p solar cells with i-layer deposited via plasma enhanced chemical vapor deposition (PECVD) with a germane to disilane ratio of 0.72 and hydrogen dilution R=(H_2 flow)/(GeH_4+Si_2H_6 flow) values of 1.7, 10, 30, 50, 120, 180 and 240 were deposited on stainless steel substrates. This germane to disilane ratio is what we typically use for the i-layer in the bottom cell of our standard triple-junction solar cells. Solar cell current-voltage curves (J-V) and quantum efficiency (QE) were measured for these devices. Light soaking tests were performed for these devices under 1 sun light intensity at 50 °C. While device with R=30 showed the highest initial efficiency, the device with R=120 exhibit higher stabilized efficiency after 1000 hours of light soaking.

Single-layer a-SiGe films (~500 nm thick) were deposited under the same conditions as the i-layer of these devices on a variety of substrates including 7059 glass, crystalline silicon, and stainless steel for visible-IR transmission spectroscopy, FTIR, Raman scattering and hydrogen effusion studies. It is interesting to note that: 1) with increasing R the H content in the a-SiGe films decreases, based on both the IR and H effusion measurements; 2) while the H content changes significantly with different R, the change in E_g is relatively small. This is most likely due to a change in Ge content in the films for different R; 3) the phase transition from a-SiGe to μc-SiGe occurs when the film was deposited on glass with R around 180.

3.1.2 INTRODUCTION

Although the correlation between amorphous silicon based solar cell device performance and a variety of intrinsic layer (i-layer) material properties have been studied broadly,[1,2,3] a reliable correlation between i-layer properties and device performance is not yet well established. This is partially due to the different ways used for depositing these materials. H dilution has been used extensively to improve a-Si based solar cell materials and device quality.[4,5,6] However, the exact role of H dilution to the growth of narrow bandgap a-SiGe alloys, in particular the phase transition from amorphous to microcrystalline state of the materials, have not yet been fully understood and deserve further study. Here we describe our recent studies of a-SiGe n-i-p solar cells and films deposited under a wide range of H dilution. We were particularly interested in the phase transition region and the effect of the different hydrogen dilution on long-term stability of these solar cells.

3.1.3 EXPERIMENT

A-SiGe films, approximately 0.5 μm thick, were deposited on 7059 glass, c-Si substrates and stainless steel (SS) using a hydrogen dilution ratio R of 1.7, 10, 30, 50, 120, 180 and 240 by PECVD. Optical measurements were performed for samples on

7059 glass substrates to obtain sample thickness, refractive index and the bandgap. FTIR absorption measurements were taken for samples on c-Si substrates to obtain information on the H content and bonding. In order to analyze the structural properties, Raman scattering spectra were measured for the films on 7059 glass and for cell devices on stainless steel, upon excitation of an argon laser with 488nm wavelength. H effusion measurements were performed on samples deposited on SS substrates to obtain the total H content.

Single junction n-i-p solar cells using these a-SiGe materials as the i-layers were deposited on SS substrates without the use of a back-reflector. I-V measurements were taken under a Xe-lamp solar simulator under AM1.5 spectrum. Quantum efficiency (QE) measurements were taken between 420 nm and 900 nm. Light soaking was performed under one-sun light intensity using a metal halide lamp. The intensity is maintained at a level so that a reference Si solar cell generates the same current as it does under a Xe-lamp simulator.

3.1.4 RESULTS

3.1.4.1 Single-layer a-SiGe films

Table 3-1 shows the deposition conditions for these a-SiGe films including the flows of GeH_4, Si_2H_6 and H_2, the substrate temperature, radio frequency power, chamber pressure, and deposition time. The deposition times of our single layer films were adjusted so that the samples would have approximately the same thickness. It is worth noting that Sample GD422 is made using the dilution that is currently used for the bottom cell i-layer and, therefore, serves as a reference point for this set of samples.

Transmission spectra of the single layers were measured using dual beam visible/near-IR spectroscopy. No substrate was used in the reference beam during the measurement. There were clear interference fringes within the measured range allowing us to calculate the refractive index *n* in the weak absorption region and the thickness *d* for the samples.[7] A linear fit to the refractive index *n* plotted versus $1/\lambda^2$ allows us to extrapolate the *n* value in the strong absorption region (λ<800nm). The *n* values estimated from this extrapolation were then used together with the transmission values in the strong absorption region to obtain absorption coefficient α. A linear fitting of the Tauc plot, $(\alpha h\nu)^{1/2}$ vs. $h\nu$, gives the material's bandgap E_g.

Using the above procedure, *n*, *d*, and E_g for all of the samples with different R were measured and summarized in Table 3-2. The deposition rates were obtained from the thicknesses and deposition times. It is found that the deposition rate is reduced by more than one order of magnitude when R is increased from 1.7 to 240.

To find out H content and the bonding configuration, infrared absorption for these films were measured using an FTIR spectroscope. There were two absorption peaks observed near 640 and 2000 cm^{-1}, corresponding to the waging and stretching modes of Si-H and Ge-H bonding. From the 640 cm^{-1} peak we calculated the H content. We find that the H content decreases with increasing R. Sample GD419 (with R=1.7) has the largest amount of H. While there is a pronounced peak near 2100 cm^{-1} for the low R sample (GD 419), the stretching mode absorption for the high R sample (R=120) shows only 2000 cm^{-1} absorption indicating mostly monohydride bonding.

Table 3-1. Deposition conditions for the single i-layer including process gas flow rates, temperature, radio-frequency power, chamber pressure, and deposition time.

Sample	R	GeH4	Si2H6	H2	Temp	Power	Pressure	Time
No.		(sccm)	(sccm)	(sccm)	(C)	(W)	(Torr)	(min)
GD419	1.7	0.72	1	2.9	400	3	0.6	30
GD420	10	0.72	1	17.2	400	3	0.6	60
GD422	30	0.72	1	51.6	400	3	0.6	120
GD423	50	0.72	1	86.0	400	3	0.6	180
GD424	120	0.72	1	202	400	3	0.6	240
GD449	180	0.468	0.65	202	400	3	0.6	360
GD450	240	0.35	0.49	201	400	3	0.6	480

Table 3-2. Results of measurements on single i-layer films including thickness of film, index of refraction, bandgap, and hydrogen content.

Sample No.	R	Thickness (nm)	Dep.rate (nm/sec)	n@600nm	E_g (eV)	[H] from IR (at.%)	H effusion relative
GD419	1.7	529	0.294	4.42	1.515	15.4	13.8
GD420	10	531	0.148	4.45	1.489	12.4	9.7
GD422	30	556	0.0772	4.36	1.479	10.9	13.2
GD423	50	608	0.0563	4.29	1.482	8.6	7.9
GD424	120	410	0.0285	4.48	1.516	11.6	7.6
GD449	180	492	0.0227	4.47	1.501	5.1	--
GD450	240	511	0.0177	4.53	1.482	4.7	--

Figure 3-1 shows the H effusion spectra of these a-SiGe films. The partial pressure of H is measured during pumping so the H content is proportional to the integrated area under the curves. A relative value from the integrated area is shown in Table 3-2. Again, we see that the H content decreases with increasing R. It is interesting to note that while H content is decreased significantly, the bandgap remains approximately the same. This suggests that the Ge contents in the high R samples are likely lower. Another point worthy discussion is the sudden decrease in H content when R is increased to 180, implying the occurrence of phase transition from amorphous state to microcrystalline state.

To clarify this structural variation we performed Raman spectroscopy measurements on the three samples with highest dilution. Figure 3-2 shows the Raman spectra of sample GD424, GD449 and GD450, taken from the front surface of the a-SiGe films on 7059 glass. And for comparison the Raman spectrum of GD450R, taken from the back- side of sample GD450 through the glass substrate, is also shown in the figure.

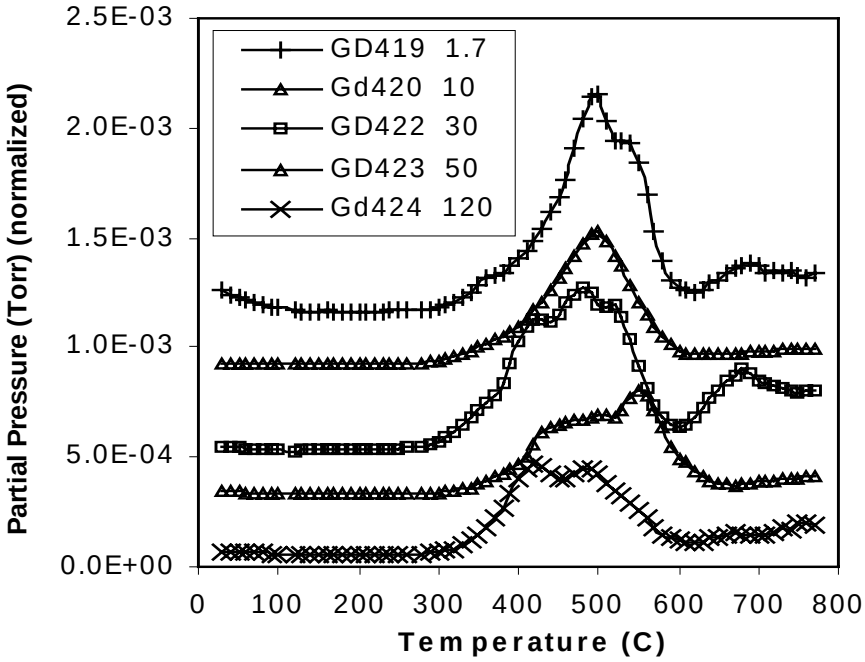

Figure 3-1. Results of H effusion experiments performed under differential pumping. Total H content is the area under the curve.

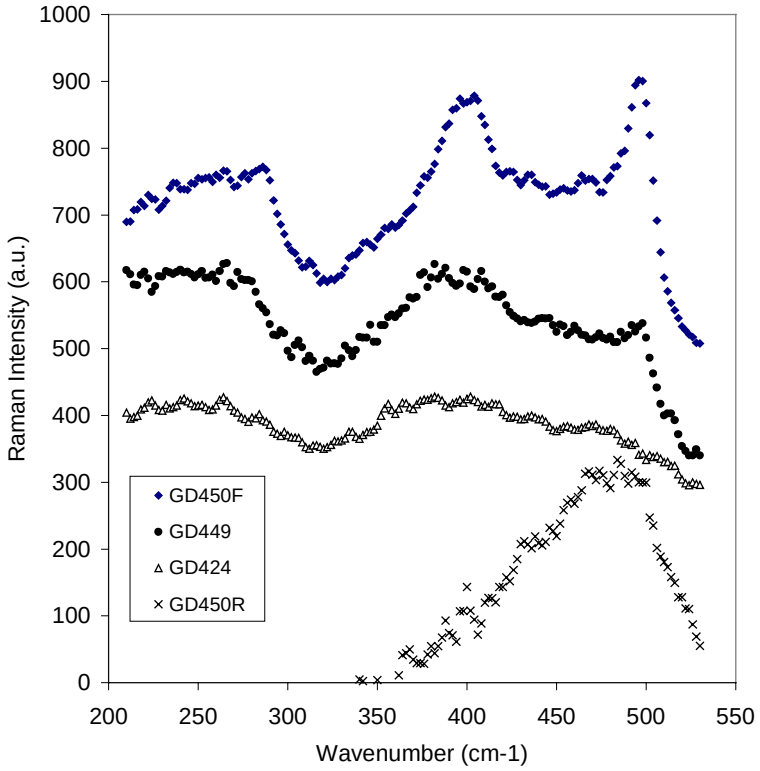

Figure 3-2 The graph shows the Raman spectra of sample GD424, GD449 and GD450 on 7059 glass. For GD450 we have taken the signals from both sides, the front- and back-side of the sample, denoted as GD450F and GD450R, respectively.

From these spectra, several Raman characteristic peaks can be seen. For sample GD424 (R=120), two broad peaks were observed at ~390cm^{-1} and ~260cm^{-1}, which may correspond to Si-Ge and Ge-Ge vibrations in the amorphous network. Compared to the earlier report[7a] on Raman spectra of a-SiGe, these peaks have a red shift of about 10cm^{-1}, probably due to more Ge contents in our samples. In addition to the above two peaks, a shoulder at ~470cm^{-1} was recognized, which corresponds to the TO phonon of a-Si, while with 10cm^{-1} red shift with respect to the normal a-Si TO phonon. This lowered frequency could be due to the presence of the larger mass neighboring Ge atoms in the amorphous network.

As R increases to 240 (GD450), the crystallized SiGe Raman characteristic peaks were observed: the Si-Si TO phonon at 498cm^{-1}, the Si-Ge vibration at 400cm^{-1} and Ge-Ge TO phonon at 286cm^{-1}. This observation is similar to the results reported by Jelenkovic et al[7b], who obtained the three Raman peaks from the SiGe samples deposited by sputtering and crystallized at 550°C, while our results are based on the microcrystalline SiGe samples prepared only by H-dilution in PECVD.

For sample GD449 with R=180, we find that it is near the phase transition region from amorphous to microcrystalline state. When R is increased up to 180, the Si-Si vibration at 498cm^{-1} starts to appear in the Raman spectrum, while the Si-Ge vibration at 400cm^{-1} keeps nearly unchanged. Similar situation was also observed by Jelenkovic et. al. They found that during annealing crystallization the Si-Si peak first appeared and grew in intensity with annealing time (see their Fig.4). It seems that there are phase segregation phenomena in a-SiGe films and the crystallization begins first from the Si-rich region. Further study is needed to clarify this assumptions.

For the Raman spectrum GD450R, taken from the back-side of GD450 through the glass substrate, only one broad peak can be seen at 480cm^{-1}, indicating that the film first grown on the glass substrate is still in amorphous state, even though R is as high as 240. Crystallinity of SiGe films deposited in PECVD process with a high hydrogen dilution depends on the film thickness.

3.1.4.2 a-SiGe n-i-p Devices

The a-SiGe films with different R were used as i-layer for n-i-p solar cells. The device structure was: SS/a-Si n^+/n-i buffer/a-SiGe absorber layer/i-p buffer/μc-Si p^+/ITO. The n-i and i-p buffer layers consisted of a-Si buffer layers next to the doped layer and a-SiGe interface layers with a graded bandgap to reduce bandgap discontinuity. The a-SiGe absorber layer had a graded bandgap such that the bandgap is narrower near the p-side.[8] Such a graded bandgap is used in the routine fabrication of bottom cells for high efficiency triple-junction solar cells. No back-reflector was used for this study since the comparative study would be expected to yield the same results with or without a back-reflector.

For all of these devices, only the i-layer conditions were varied. All other deposition conditions were kept unchanged. In order to fabricate solar cells with i-layer of approximately the same thickness, the i-layer deposition time was adjusted according to the thickness measurement of the single-layer sample. The thickness of the i-layer was measured using a capacitance technique. This thickness includes the thickness of both the a-SiGe absorber layer and the buffer layers. Table 3-3 shows the solar cell performance

of a series of a-SiGe solar cells deposited using different H dilution, ranging from 1.7 to 240. The photovoltaic parameters of the cells were measured under a Xenon lamp solar simulator with AM1.5 light. The QE data were summarized, including the maximum of QE, the QE values at 400 nm and 700 nm. For a-SiGe solar cells deposited on bare SS, the red response was high.

It is seen from the Table that the J_{ph} value, obtained by integrating QE curves over AM1.5 spectrum, suggest that the short circuit current is higher for R=10 to 120. The drop in J_{sc} at higher R (>120) is due to microcrystalline formation. J_{sc} values from the J-V measurement have slightly larger variation. J_{sc} is relatively low for these samples since no back-reflector is used for this study. The FF is highest (FF=59.1%) for R=30, a moderate dilution, which is the condition that we used for the fabrication of the bottom cell of our 11% triple-junction solar cell. Device GD425 (R=30) is the same as our standard bottom cells and is used as a reference for this dilution study. The V_{oc} increases from 0.64 V to 0.67 V with R up to 120, before it starts to decrease down to 0.64 V when R is further increased to 240, again due to small amount of microcrystalline phase formed at R=180, as expected from the above Raman scattering results taken from high dilution films on glass. Considering the fact that the a-SiGe solar cells are deposited on stainless steel and only 168nm (GD452) thick, the microcrystallinity may not be the same as thick films on glass. Therefore, we performed Raman measurements on the solar cells deposited on SS substrates. Fig. 3-3 gives the Raman spectra measured from the samples of GD451 and GD452. It is seen that there is a main characteristic peak at ~480cm^{-1}, indicating that these samples are mostly in amorphous state, and it seems to have a small shoulder at ~ 500cm^{-1}, showing the beginning of crystallization. However, due to experimental fluctuation, this shoulder needs to be further verified.

Table 3-3. Performance of n-i-p devices made with different H dilution R.

Device No.	H dilution R	Time (min)	Thickness (nm)	V_{oc} (V)	J_{sc} (mA/cm^2)	FF (%)	Eff (%)	QE at 400nm	QE at 700nm	J_{ph} (QE)	Light Degrad. (%)
GD429	1.7	9.5	189	0.638	13.9	53.8	5.54	0.57	0.37	13.7	>21.1
GD428	10	19	190	0.640	16.2	53.1	6.02	0.58	0.42	14.4	20.9
GD425	30	36	189	0.656	15.7	59.1	6.76	0.59	0.43	14.5	21.6
Gd426	50	50	175	0.662	15.8	55.0	6.25	0.58	0.32	14.0	14.2
GD427	120	98	190	0.669	14.9	54.8	6.25	0.60	0.39	14.3	11.4
GD451	180	123	176	0.656	15.8	56.0	6.65	0.64	0.27	13.6	--
GD452	240	158	168	0.636	14.7	55.8	6.55	0.63	0.29	13.6	--

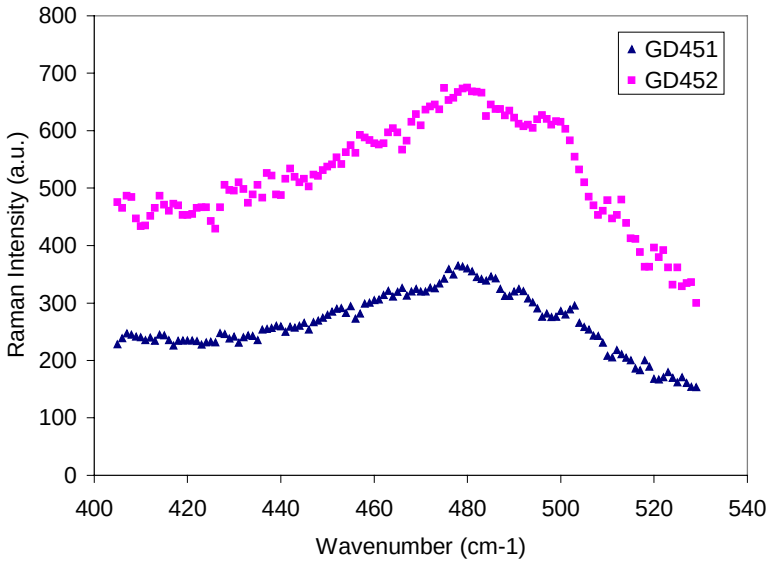

Figure 3-3 This figure shows the Raman spectra measured from the surface of the cell samples of GD451 (R=180) and GD452 (R=240) on stainless steel substrate.

3.1.4.3 Light Soaking Stability Test

Light soaking tests for these a-SiGe samples were performed to understand the effect of R on the device stability. The light soaking was done under a metal halide lamp with one-sun light intensity. This lamp is relatively blue rich and has somewhat less red light compared with AM1.5 global spectrum. Our samples are light soaked under one-sun light intensity. Since an a-SiGe bottom cell typically sees only one third of the sun light inside a triple-junction solar cell, this one-sun light intensity is approximately three times more intense than that in the standard testing conditions. However, the relative trend among these samples would likely remain the same. The last column of Table 3-3 shows the degradation under one-sun light soaking at 50 ^{o}C for 1000 hours. The degradation for sample GD429 at 1000 hours of soaking is unavailable since all of the test cells were shorted. The 300-hour soaking results shows a degradation of 21.1%, which is expected to be further increased at 1000 hours. It is found that the degradation is reduced with higher R, down from 20.9% for R=10 to 11.4% for R=120. Degradation of Samples GD451 and GD452 are not included here since they were fabricated later. From Table 3-3, one concludes that before light soaking, R=30 (GD425) shows the highest P_{max} while after light soaking, R=120 (GD427) shows the highest P_{max}.

3.1.5 CONCLUSION

We have deposited a series single-layer films and n-i-p solar cells devices using narrow bandgap (~1.5 eV) a-SiGe materials deposited via PECVD using different H

dilution ranging from R=1.7 to 240. Samples with higher R value showed lower amounts of H incorporated into the film though the bandgap remained approximately the same. This suggests that the Ge content in films deposited with higher R is likely lower. Measurements of Ge content in these films will be performed to verify this. The results from the devices and films deposited using different H dilution suggest that a high H dilution up to 120 could be used to deposit a-SiGe films with improved light stability.

3.2 Comparison study of a-SiGe films and n-i-p devices with different Ge content in the i-layer

3.2.1 Summary

In order to improve our understanding of the influence of the germanium content on the optoelectronic properties of amorphous silicon germanium alloy thin films and the performance of the n-i-p solar cells with the corresponding i-layer, we prepared and studied a series of a-SiGe films and n-i-p solar cells with varying GeH_4 to Si_2H_6 ratio in the process gas from 1.43 to 0. These silicon germanium alloys are used for making different i-layers in a multi-junction solar cell in order to capture the full range of the solar spectra. These studies help in optimizing the device performance for better efficiency and stability. Establishing such a baseline is necessary for the further improvement of our devices from our present 11% initial triple cells.

We deposited about 0.7 μm thick a-SiGe layers with varying GeH_4 to Si_2H_6 ratio, on Corning 7059 glass, crystalline silicon and stainless steel substrates. We found that as the GeH_4 to Si_2H_6 ratio in the process gas increases, the band gap E_g decreases. E_g is 1.36 eV for a GeH_4 to Si_2H_6 ratio of 1.43 (highest GeH_4 flow) while E_g is 1.84 eV for a ratio of zero (no GeH_4 flow). FTIR measurements show that the total hydrogen content (as determined by the bending mode near 600cm^{-1} including the Ge-H bending mode) increases with decreasing Ge content. In addition, films with higher Ge content are less photosensitive.

N-i-p solar cells which have i-layers corresponding to these a-SiGe films are fabricated. We observe that V_{oc} and FF increase, whereas J_{sc} decreases as the Ge content is lowered. A similar trend is observed in the QE measurements, where the integrated current J_{ph} decreases as the Ge content is decreased.

3.2.2 Introduction

Amorphous silicon germanium alloys are usually used as the bottom and middle cell i-layers in a high-efficiency triple-junction amorphous silicon alloy based solar cells. By varying the amount of Ge in the i-layer, the band gap can be varied from ~1.1eV (in pure a-Ge films) to ~1.8eV (pure a-Si films). This allows the capture of the full range of the solar spectra in different layers and thus increases the efficiency of the solar cells. However, the properties of a-SiGe alloy films and the performance of a-SiGe solar cells deposited in different laboratories or different manufacturing plants are not necessary the same. Therefore, the Ge contents in the bottom and middle cell i-layer optimal for high-efficiency triple-junction solar cell are likely different in different laboratories. In this work, we study a-SiGe alloy materials and solar cells to establish the choice of a-SiGe alloys optimal for use as the bottom and middle cell i-layers in our laboratory. Such a component cell study is important for further improving our cells with efficiency beyond our present 11% triple cells.

We have made a-SiGe films with varying amount of Ge and then used these alloys as the i-layers in fabricating single-junction solar cells. Some of these layers are standard i-layers that have been routinely used in the fabrication of our triple junction solar cells, as the bottom, middle and top cell i-layers. To find a-SiGe i-layer that yield

higher triple-cell efficiency than our current standard a-SiGe i-layers, we also explored a-SiGe alloy materials with intermediate Ge content between the bottom and middle cells and between the middle and top cells. In addition, we made some cells which have higher Ge content than our regular bottom cell.

3.2.3 Experimental Details

A-SiGe films, approximately 0.7 μm thick, are deposited on Corning 7059 glass, c-Si substrates and stainless steel (SS) with varying GeH_4 to Si_2H_6 ratio. The hydrogen flow is the same as that for our standard cells. For i-layers with the intermediate Ge content, hydrogen and Si_2H_6 flows were adjusted accordingly. Table 3-4 shows the deposition conditions for these a-SiGe films, including the flow of GeH_4, Si_2H_6, H_2, the substrate temperature, rf power, chamber pressure and deposition time. The deposition times are adjusted so that these samples have approximately the same thickness. It is to be noted that GD357, GD359 and GD361 are deposited under the same conditions as the i-layers in our regular bottom, middle and top cells, except that GD357 has no Ge grading as we have in our bottom cell. These samples serve as the reference points for this set of samples. N-i-p solar cells using these a-SiGe materials as the i-layers are deposited on SS with and without a Ag/ZnO back reflector. J-V measurements are taken under a Xenon solar simulator.

Table 3-4 Deposition conditions for a-SiGe films with different Ge contents.

	Used in	GeH_4	Si_2H_6	H_2	Temp	Time	Power	Pressure	GeH_4/Si_2H_6	$H_2/\{Si_2H_6+GeH_4\)$
	triple-cell	(sccm)	(sccm)	(sccm)	(C)	(min)	(W)	(Torr)		R
GD431		1.00	0.7	50	400	180	3	0.6	1.43	32
GD430		0.80	0.8	50	400	180	3	0.6	1	33
GD357	bottom	0.72	1	50	400	180	3	0.6	0.72	30
GD358		0.63	1.25	60	350	180	3	0.6	0.504	33
GD359	middle	0.54	1.5	70	300	180	3	0.6	0.36	35
GD360		0.27	1.5	72.5	250	240	2.25	0.6	0.18	42
GD361	top	0	1.5	75	200	300	2.5	0.6	0	50

3.2.4 RESULTS AND DISCUSSION

3.2.4.1 Single layer amorphous silicon germanium films

Figure 3-4 shows the transmission spectrum of a typical sample GD357, which is deposited using the same GeH_4/Si_2H_6 ratio as our standard bottom cell i-layer. This transmission spectrum is measured using a dual beam visible/near IR spectroscopy. No substrate is used in the reference beam during the measurements. In the spectrum, there are clear interference fringes within the measured range. The refractive index n in the

weak and medium absorption region and the thickness *d* for these samples are calculated from the position of these interference fringes and their transmission values.[7] In Figure 3-5, the refractive index *n* as a function of $(1/\lambda^2)$ is plotted. A linear fitting allows us to extrapolate the n values in the strong absorption region. The *n*-value estimated from this extrapolation is then used together with the transmission values in the strong absorption region to obtain the absorption coefficient α.

Figure 3-6 is the Tauc plot $(\alpha h\nu)^{1/2}$ vs $h\nu$, for the sample in the range 590-750nm (for GD357). A linear fitting of the plot gives material's bandgap. A fitting with better *R*-squared value could be obtained using a smaller fitting range, which gives a slightly higher E_g value. However, as long as the fitting procedure is consistent, the conclusion for this study remains unaffected.

Using the procedure described above, *n*, d and E_g for all of the samples with different [Ge] are measured and summarized in Table 3-5. The deposition rates are obtained from the thickness and deposition times. It is found that the deposition rate is reduced by nearly about 50% when GeH_4/Si_2H_6 ratio decreases from 1.43 to 0. This is because the films with less GeH_4 flow are prepared with higher hydrogen dilution. Figure 3-7 shows E_g vs GeH_4/Si_2H_6 ratio for these films.

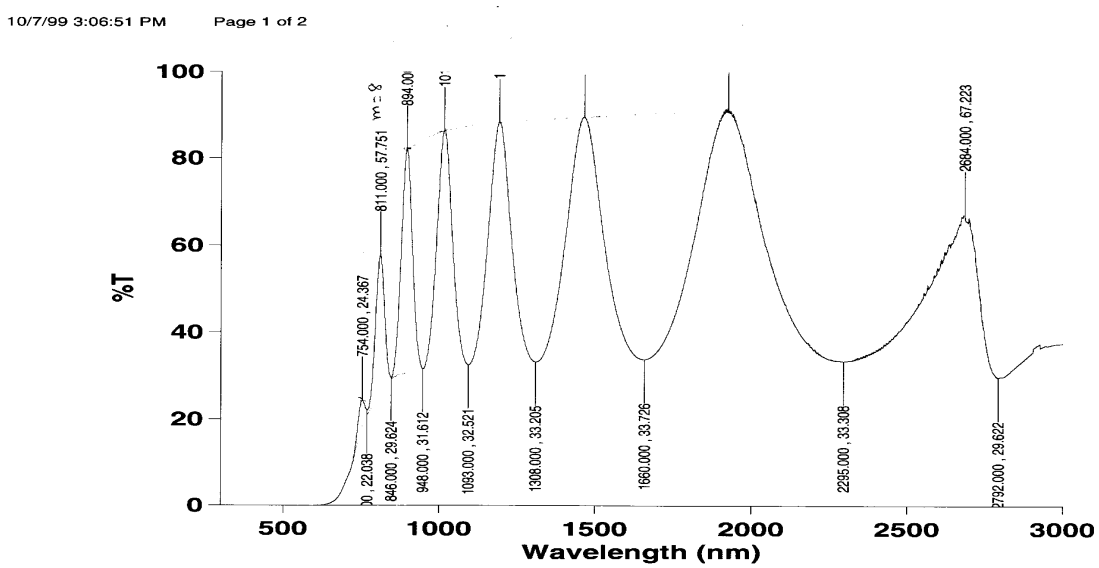

Figure 3-4. Transmission spectrum of a typical a-SiGe film (GD357).

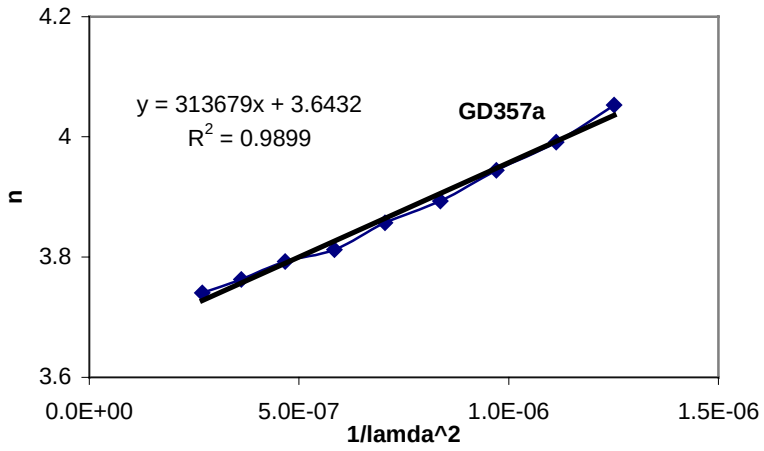

Figure 3-5. Refractive index as a function of $1/\lambda^2$.

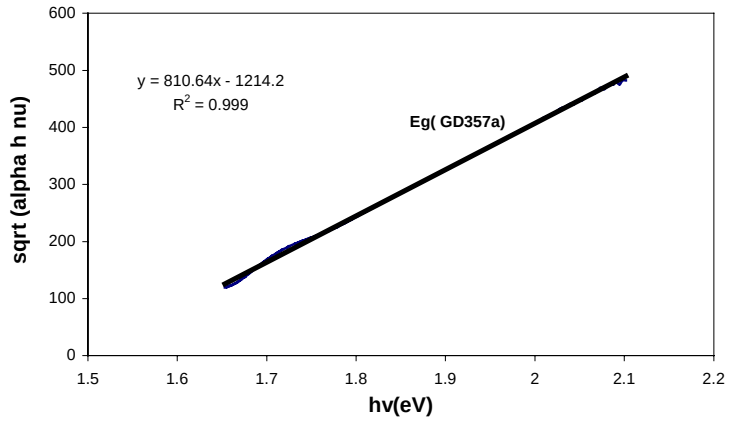

Figure 3-6. Tauc plot, $(\alpha h\nu)^{1/2}$ vs $h\nu$, used to determine the bandgap E_g.

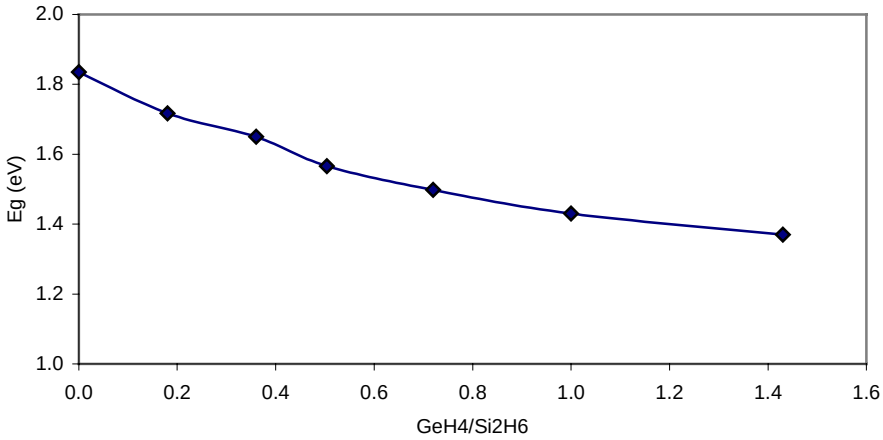

Figure 3-7. The bandgap E_g of a-SiGe films as a function of GeH_4 and Si_2H_6 gas ratio during deposition.

Table 3-5. Film properties n, d, and E_g for a-SiGe films with different Ge content.

Sample	GeH_4/Si_2H_6	H dilution R	Thickness (nm)	Dep rate (nm/sec)	E_g (eV)	n at 600nm	[H] (at.%)
GD431	1.43	32	720	0.0666	1.37	4.81	8.6
GD430	1.00	33	720	0.0666	1.43	4.49	7.8
GD357	0.72	30	772	0.0715	1.50	4.59	10.5
GD358	0.50	33	774	0.0716	1.57	4.62	11.9
GD359	0.36	35	741	0.0686	1.65	4.27	15.0
GD360	0.18	42	774	0.0538	1.72	4.60	18.1
GD361	0.00	50	727	0.0404	1.84	4.06	16.5

Following the work of Mckenzie et al. [1991], we try to estimate the amount of Ge in these films. We use E_g=1.76-0.78x for a-$Si_{1-x}Ge_x$. to estimate the x for samples Gd431, Gd430, GD357, and Gd358. Whereas, the correction for the band gap for pure amorphous silicon film has been done keeping in mind that these films are prepared with higher hydrogen dilution and at lower temperature. The estimated Ge content as a function of E_g is plotted in Figure 3-8.

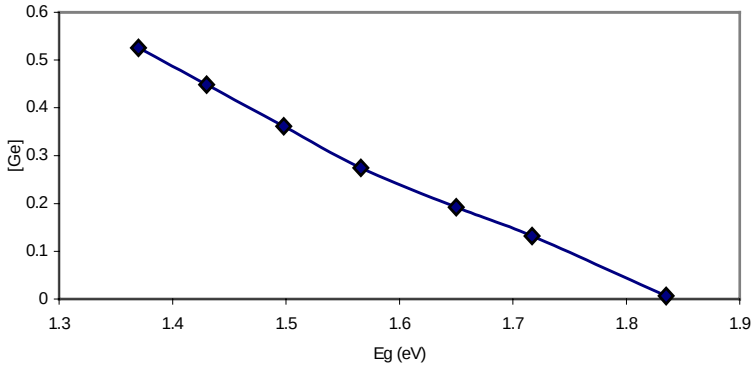

Figure 3-8. Ge content estimated from the bandgap.

FTIR Measurements

To find out the H content and its bonding in our films, infrared absorption for these films is measured using an FTIR spectroscope in the range of 400-4000cm^{-1}. Figure 3-9 shows the transmission of these a-SiGe films in the 400-2400 cm^{-1} range.

The crystalline silicon substrate from the same plot has been used to determine the baseline for these measurements. The curves in Figure 3-9 are shifted vertically for clarity. There are absorption peaks near 640 and 2000 cm^{-1}, corresponding to the wagging and stretching modes of Si-H (or Ge-H) bonding. In Figure 3-10, the absorption curves in the range 400-850cm^{-1} are plotted to show the Si-H and Ge-H wagging mode absorption. H content calculated from the wagging mode absorption is shown in Table 3-5. Figure 3-11 shows the smoothened curves of FTIR transmission in the range of 1800-2200cm^{-1} to illustrate the features of Si-H and Ge-H stretching modes.

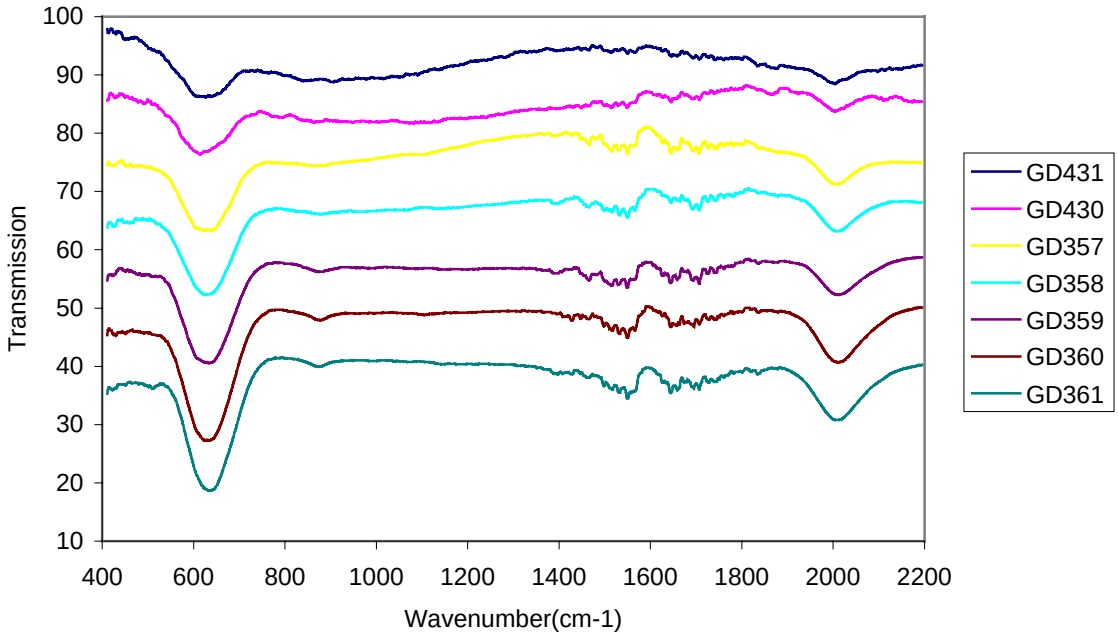

Figure 3-9. FTIR spectra of a-SiGe films with different Ge content.

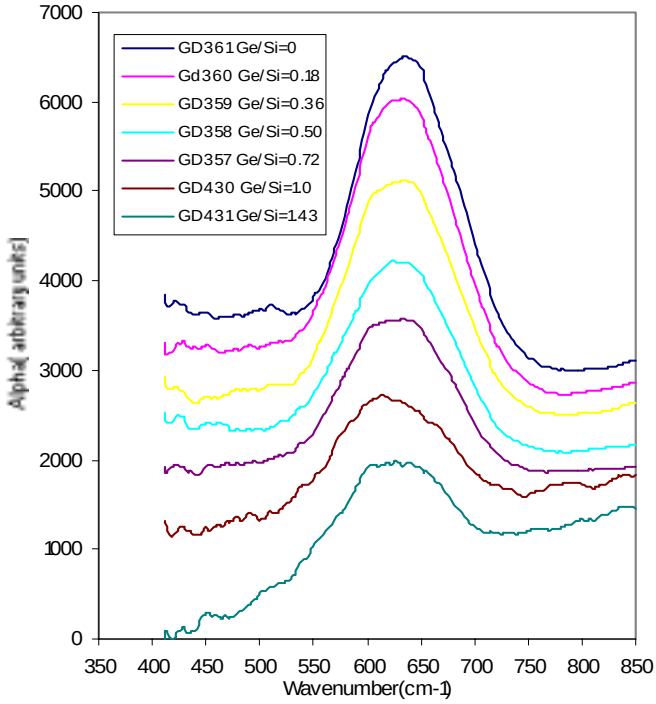

Figure 3-10. FTIR spectra in the 420-850 cm^{-1} range, showing the wagging mode of Si-H (640 cm^{-1}) and Ge-H (560 cm^{-1}).

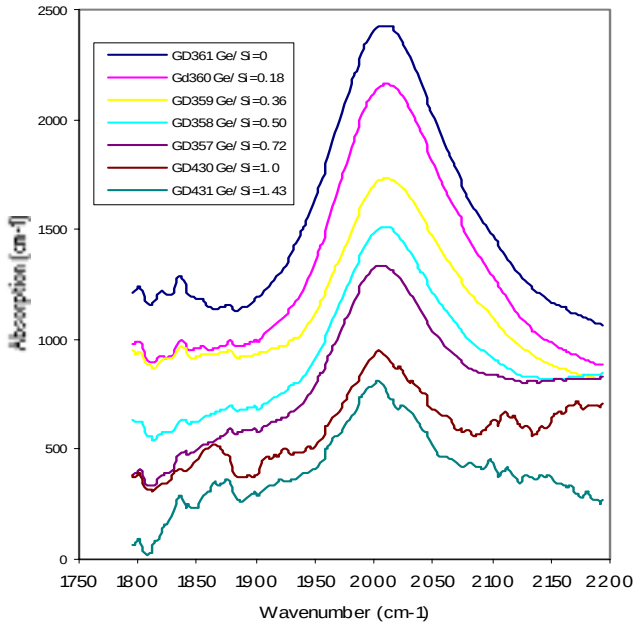

Figure 3-11. FTIR spectra in the 1800-2200 cm^{-1} range, showing the stretching mode of Si-H (2000 cm^{-1}), Si-H_2 (2100 cm^{-1}) and Ge-H_2 (1975 cm^{-1}).

Conductivity Measurements

Preliminary dark and photoconductivity measurements on GD357-Gd361 show that the dark conductivity of these films decreases as [Ge] content decrease in these films, however, when [Ge] decreases, these films become more photosensitive, i.e., the photoconductivity to dark conductivity ratio increases upon decreasing [Ge], or in other words, increasing the band gap of these films. Figure 3-12 Shows the photosensitivity as a function of bandgap for these films under a tungsten lamp. (Intensity less than AM1.5).

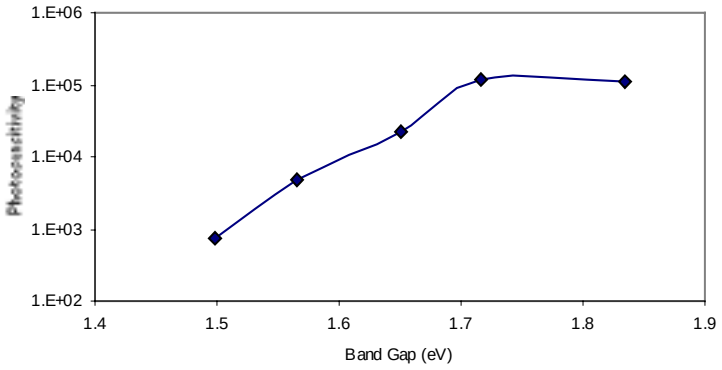

Figure 3-12. Photosensitivity of a-SiGe films as a function of a-SiGe bandgap for this series of a-SiGe films.

3.2.4.2 A-SiGe n-i-p Devices

These a-SiGe films with varying [Ge] are then used as i-layer for n-i-p solar cells. The device structure is: SS/a-Si n^+/n-i buffer/a-SiGe absorber layer/i-p buffer/μc-Si p^+/ITO. The n-i and i-p buffer layers consist of a-Si buffer layers in between a doped layer and the absorber layer. Unlike our normal cells, these buffer layers did not have any graded bandgap. The Si-Ge absorber layer, also was prepared without any germanium grading to match with the corresponding single layer films.

Table 3-6 shows the selective i-layer deposition conditions for these a-SiGe solar cells. For all these cells, the n^+ and p^+ layers remain the same, whereas the buffer layers were prepared at the absorber layer temperature for the same duration for all the samples. The deposition time for absorber layer for these cells was estimated from the deposition rate of the single layers so that all the samples have the same thickness. However, partially because of the non-uniform deposition on a 4"x 4" substrate and partially because of the fact that the buffer layers were prepared at different temperatures, we find a variation in the thickness of these cells. The thickness of i-layer is measured using capacitance measurement technique and is also included in the table.

Table 3-6. Deposition conditions for the i-layers of a-SiGe solar cells.

	Used in triple	GeH_4 Sccm	Si_2H_6 sccm	H_2 sccm	Time (min)	Thickness (nm)	GeH_4/Si_2H_6	H dilution R
gd441		1.00	0.7	50	42.0	151	1.43	32
gd442		0.80	0.8	50	42.0	184	1.00	33
gd443	bottom	0.72	1	50	39.2	171	0.72	30
gd435	bottom	0.72	1	50	37.3	153	0.72	33
gd436		0.63	1.25	60	39.1	171	0.50	33
gd437	middle	0.54	1.5	70	40.9	209	0.36	35
gd438		0.27	1.5	72.5	52.1	215	0.18	42
gd439	top	0	1.5	75	69.3	194	0.00	50

Figure 3-13 shows a representative J-V curve of a cell in a sample GD435 (GeH_4/Si_2H_6 =0.72, average Ge content in our standard bottom cell with graded Ge) measured under a Xenon lamp solar simulator at an intensity of 100 mW/cm^2. This device shows a V_{oc} 0.674V, a J_{sc} of 18.1mA/cm^2, a FF of 56.8 and a P_{max} of 6.94 mW/cm^2 corresponding to an efficiency of 6.94%. These values are comparable to our standard solar cells with graded buffer layer and absorber layer. The slight decrease in maximum power may be due to the bandgap discontinuity at the interface of these low bandgap cells. For each device fabricated, there are 23 cell of 0.05cm^2 size. Three cells with highest P_{max} are selected to represent the device performance. The average performance of the three cells is used for sample comparison and process optimization.

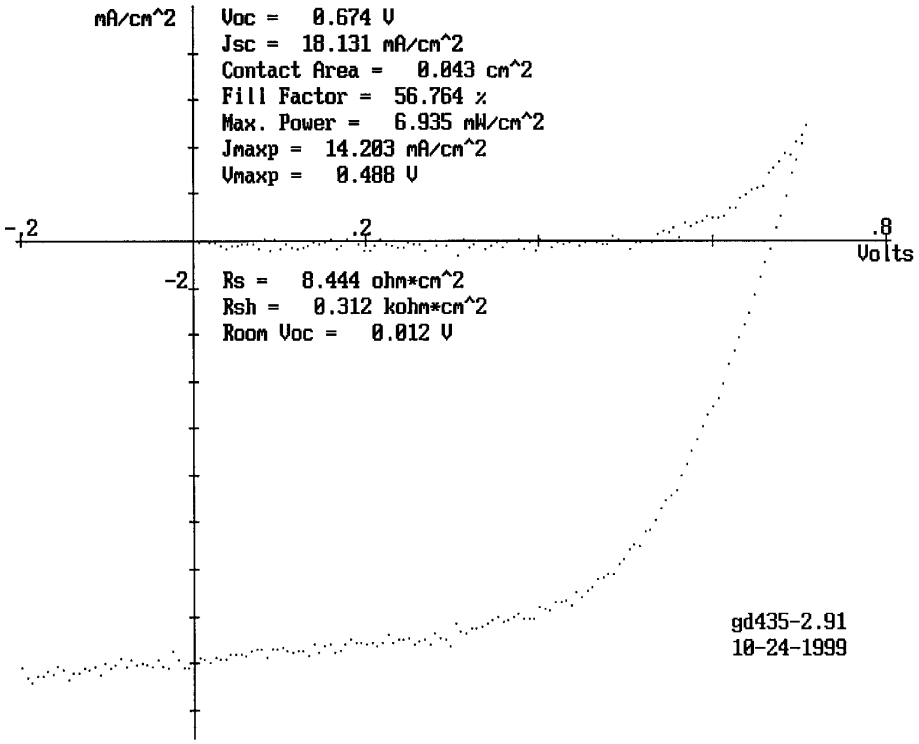

Figure 3-13. J-V curve of a representative cell (GD435) among the series, which is similar to the bottom cell in a triple-cell.

In Table 3-7, we summarize the average performance for all of the a-SiGe devices with different [Ge]. The two samples Gd435 and 443 are prepared using identical conditions at the two extreme ends of the series and their performance show that they are comparable thus a good reproducibility could be established between the different runs using the same preparation conditions. In Table 3-7, only the average performance for three cells showing highest P_{max} for each sample is listed. As we see from the table, the V_{oc} and FF increase, whereas J_{sc} decrease as [Ge] content is reduced in these cells.

Table 3-7. Performance of a-SiGe devices with different Ge content.

Sample No.	Cell	GeH_4/Si_2H_6	V_{oc} (V)	J_{sc} (mA/cm^2)	FF (%)	R_s ($Ohm*cm^2$)	P_{max} (mW/cm^2)
GD441-2		1.43	0.519	15.4	43.1	12.7	3.44
GD442-2		1.00	0.577	16.1	50.1	9.7	4.65
GD443-2	bottom	0.72	0.660	15.3	55.3	9.9	5.58
GD435-2	bottom	0.72	0.666	16.0	54.3	9.2	5.79
GD436-2		0.50	0.744	13.0	63.9	8.8	6.18
GD437-2	middle	0.36	0.810	14.2	61.8	9.3	7.11
GD437-4	middle	0.36	0.811	14.3	60.1	10.7	6.97
GD438-2		0.18	0.849	10.5	63.1	10.7	5.63
GD439-2	top	0.00	0.895	8.93	69.5	10.6	5.55
GD439-4	top	0.00	0.892	8.93	66.4	11.7	5.29

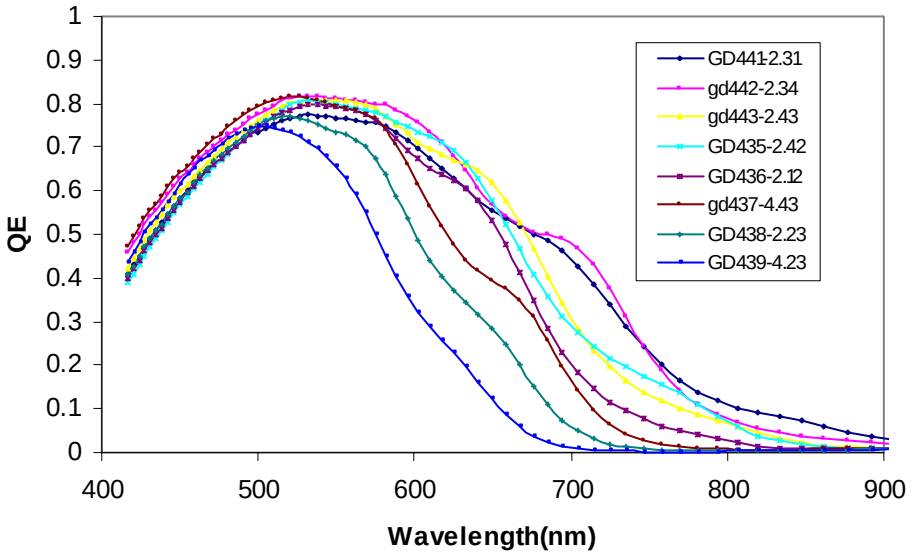

Figure 3-14. Quantum efficiency of a-SiGe solar cells with different Ge content.

The quantum efficiency for this set of devices with different [Ge] are also measured. Figure 3-14 shows the quantum efficiency curves measured in a way that the monochromatic light beam is focussed inside the cell. Therefore, the measurement is independent of the variation in the sample size. For films with higher [Ge], red response

is higher. A slight variation in the interference fringes of the quantum efficiency curves is due to the variation in the thickness of the film. Figure 3-15 shows the integrated current density J_{ph} as a function of the bandgap of absorber layer in these devices. The J_{ph} values are lower than the J_{sc} values obtained from J-V curves since 1) J_{ph} is integrated with a narrower spectral range (420nm-900nm) for these samples and 2) some light might not be focused inside the $0.05cm^2$ cell area during QE measurement. The J_{ph} values for the two samples deposited on back-reflector, shown in Figure 3-14, is not included in Figure 3-15.

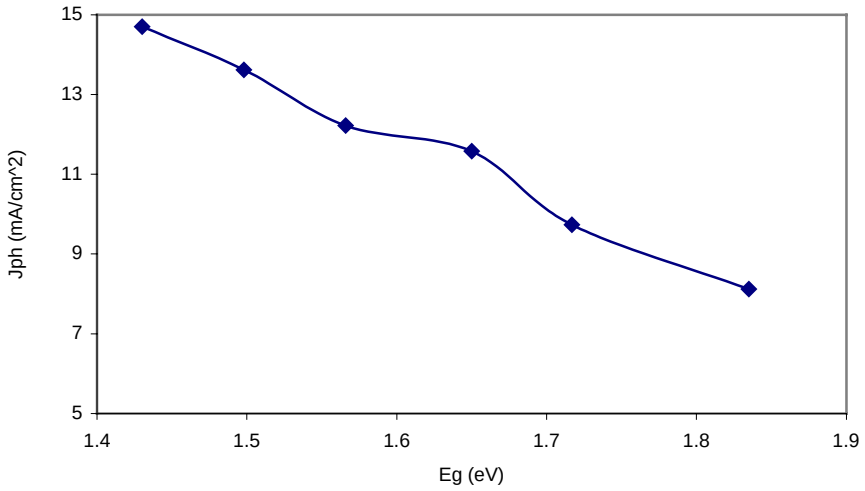

Figure 3-15. Current integrated from QE for a-SiGe cells, deposited on bare SS, with different bandgaps.

3.2.4.3 Light soaking stability study

Light degradation study has been performed for these a-SiGe solar cells with different Ge contents. These devices were put under One-sun light at around 50 °C for 1000 hours. While all V_{oc}, J_{sc} and FF degrade after 1000 hours of light soaking, we present in Figure 3-16 and 3-15 the degradation of FF as a function of the Ge content. Figure 3-16 shows the FF before light soaking for different samples while Figure 3-17 shows the percentage drop in FF. We found that devices with small amount of Ge degrades the most, while device with more Ge in the film degrades less, after 1000 hours of light soaking. One should note that the degradation is performed under 1 sun light while a bottom a-SiGe cell usually sees one third of one sun light inside a triple cell.

It is somewhat surprising to note that among this set of devices, pure a-Si device without Ge has lower light degradation than a-SiGe with small amount of Ge. Further study is to be performed to confirm this and to quantitatively describe the change of light degradation near this level of Ge alloying.

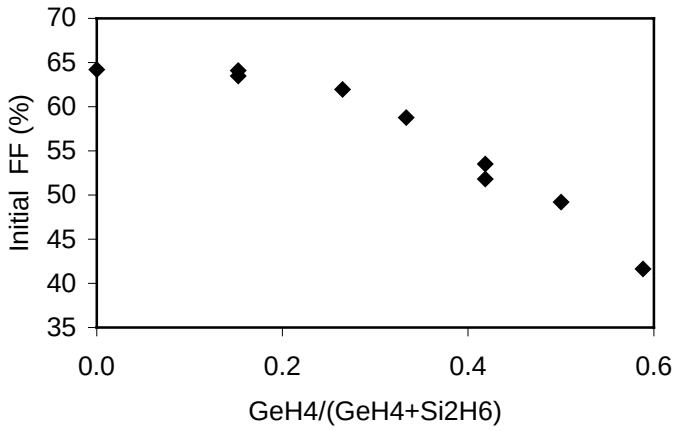

Figure 3-16. Fill factor before light soaking for a-SiGe devices with different Ge.

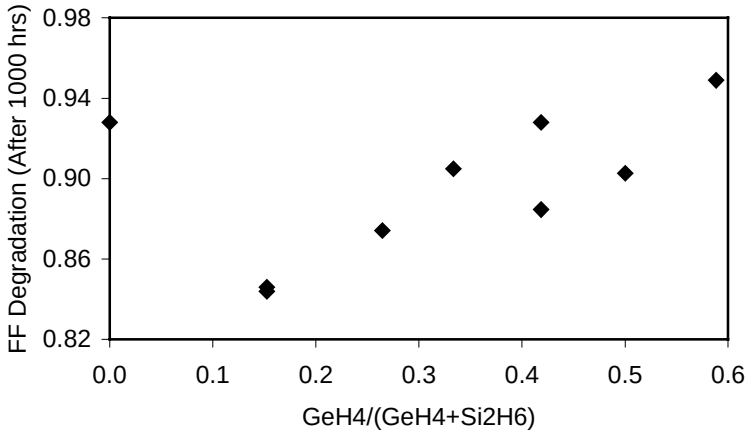

Figure 3-17. Degradation of FF for devices with different Ge.

3.3 Amorphous silicon solar cells deposited on ultra-thin SS substrate

3.3.1 Summary

To significantly reduce the solar cell weight and increase its specific power for space application, we deposited a-Si thin film solar cells on ultra-thin stainless steel (SS) substrates of 15μm, 12.5μm and 7.5μm thick and compared the results with those on standard 5 mil. (127μm) thick SS substrates that we use on a regular basis. To handle these ultra thin SS foils throughout the device fabrication process, we used a carrier method by attaching the ultra-thin SS foils on thicker 127μm SS substrates. We obtained ultra-lightweight solar cells that have similar performance as solar cells on regular 127 μm substrates, with a V_{oc} of 0.887 V, a J_{sc} of 10.8 mA/cm^2, a FF of 68% and an efficiency of 6.5% for cells without back-reflector. These 6.5% efficient, rollable solar cells deposited on 7.5μm thick SS substrates exhibit a specific power of 1.08 kW/kg, significant for space power applications and terrestrial applications such as portable electronics batteries.

3.3.2 Introduction

Thin film amorphous silicon (a-Si) based solar cells have become attractive alternatives for space power applications due to their low-cost processing and light weight [10,11] as well as their tolerance under high radiation.[12] The weight advantage of a-Si solar cells comes from their low thickness and high absorption constant. However, this weight advantage can only be realized if the substrate on which the solar cells are deposited is also reduced in weight. Several studies have been made in depositing a-Si based solar cells on lightweight substrates. Early in 1988, Hanak *et al* at Sovonics reported the achievement of 250W/kg solar arrays using a-Si deposited on lightweight flexible substrates.[10] More recently, Guha *et al* at United Solar reported 12% total-area efficiency under AM0 illumination for a-Si solar cells. Similar efficiency was obtained for cells deposited on 0.5 mil thick SS and 2-mil thick Kapton substrates.[13]

We performed a study to deposit a-Si solar cells on ultra-thin stainless steel (SS) substrates (down to 7.5 μm) for space power applications. We also report our recent results on the fabrication of a-Si based thin film solar cells on these SS substrates. These thin SS substrates are extremely light weight. In addition, it does not degrade at high temperature, allowing us wider parameter space during the thin film deposition and solar cell fabrication process. Different types of ultra-thin SS substrates are explored and summarized here.

3.3.3 Experimental

Single-junction a-Si n-i-p solar cells are fabricated in this study using an ultrahigh vacuum, multi-chamber, load-locked PECVD system. The device structure used in this study is SS/a-Si n^+/a-Si i/μc-Si p^+/ITO. No current-enhancing back-reflector is used since relative comparison is more emphasized here. Evaluation of the solar cells include solar cell I-V measurement, quantum efficiency measurement and also an estimate of fabrication yield by counting the number of cells functional within a 2”x2” sample.

Three different types of thin SS substrates are explored. These substrates, purchased from Goodfellow Corporation, include:
1) 15-μm thick AISI304 SS foil, as rolled,
2) 12.5-μm thick AISI 321 SS foil, hard; and
3) 7.5-μm thick AISI316 SS foil, as rolled.

Stainless steel substrates, 127 μm thick (5.00 mil.), obtained from ECD, are used for comparison in this study. For a fair comparison, various substrates are put in the same deposition run during the solar cell fabrication. A carrier method is used for handling these thin SS foils during fabrication. In this method, the ultra-thin SS foils are attached to (by wrapping around) thick (127μm) SS carrier throughout the fabrication process.

3.3.4 Results

Table 3-8 shows the J-V performance of the three most recent deposition runs for a-Si single-junction solar cells deposited on different substrates. All three runs were made using identical deposition conditions for n, i, p and ITO layers. These deposition conditions are the same as those used for the top cell in 11% triple-junction solar cells [14,15] except the i-layer thickness, which is around 200 nm in this study. Four pieces of 2"x2" substrates, mostly of different types, are loaded in each run for comparison. 23 cells (or 39 cells) are processed in each 2"x2" sample. By counting the number of cells functionally alive (with FF>60%), we obtained information regarding the dependence of process yield on the use of different substrates. The I-V performance listed in Table 3-8 is the average performance of the three cells with highest FF in the sample. The uncertainties in V_{oc}, J_{sc} and FF values are approximately 1%, 10% and 2%, respectively. The relatively larger uncertainty in J_{sc} is due to the small size of the solar cells (0.05 cm^2). The J_{sc} values for these solar cells with 200 nm thick i-layers are relatively low due to the lack of a current-enhancing back-reflector.

Table 3-8. Average I-V performance under AM1.5 illumination and yield information for a-Si solar cells deposited on different thin SS substrates.

Device	**Substrate**	**Average I-V performance**				**Yield**	
	Thickness (μm)	V_{oc} (V)	J_{sc} (mA/cm^2)	FF (%)	Eff (%)	Cells alive	Total cells
Gd479-1	7.5	0.906	10.0	66.0	6.0	5	23
Gd479-2	127	0.891	10.8	68.9	6.7	22	23
Gd479-3	15	0.889	11.0	63.1	6.2	12	23
Gd480-1	7.5	0.887	10.8	68.0	6.5	12	23
Gd480-2	127	0.889	10.9	69.0	6.7	7	23
Gd480-3	15	0.892	10.7	62.6	6.0	5	23
Gd480-4	127	0.864	10.0	65.0	5.6	7	39
Gd481-1	7.5	0.885	10.7	66.1	6.3	11	39
Gd481-2	15	0.895	10.3	64.3	5.9	3	39
Gd481-3	12.5	0.886	10.9	64.1	6.2	10	39
Gd481-4	127	0.889	11.4	66.4	6.7	21	39

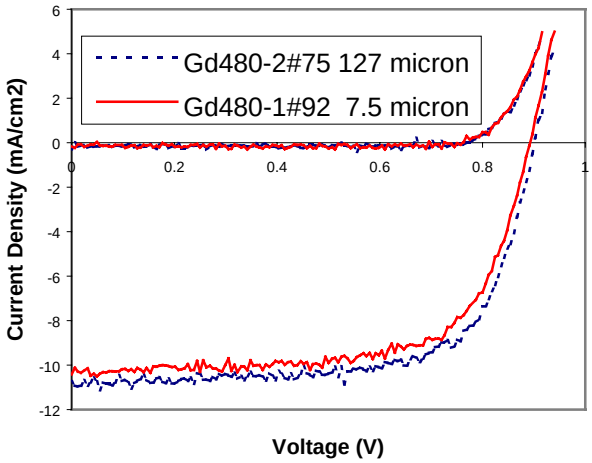

Cell	Gd480-2#75	Gd480-1#92
Substrate	127 μm	7.5 μm
V_{oc} (V)	0.901	0.893
J_{sc} (mA/cm^2)	10.7	10.4
FF (%)	70.4	68.7
Efficiency (%)	6.81	6.39

Figure 3-18. J-V curves of two representative a-Si solar cells deposited on 7.5μm ultra-thin SS substrate and 127μm thick standard SS substrate, showing very similar performance under AM1.5 illumination.

As we see from Table 3-8 and Figure 3-18, the solar cell performances for devices on different substrates are similar. Samples deposited on 127 μm thick substrates generally show slightly higher FF than samples on other substrates in the same run, leading to the highest efficiency. Comparing the thinner substrates, samples on 7.5μm thick substrates outperform those on 15 and 12.5 μm substrates, especially in the FF. Figure 3-18 shows the J-V curves of one typical cell in each of a 127μm sample (Gd480-2) and a 7.5μm sample (Gd480-1). Both samples show very similar performance within statistical variation.

The fabrication yield, number of cells alive divided by the total number of cells processed, for these samples show that 127 μm thick substrate lead to slightly higher yield. And the cells on the three-types of thin SS substrates show similar yield within statistical fluctuation.

To find out the cause for the dependence of the process yield on the substrate, we examined the different types of substrates using SEM. The SEM graphs show that both the 7.5 μm and 127 μm substrates are smoother while 12.5 μm substrates show more roughness or cracks. The 15 μm substrates appear to be somewhere in between. This may to some extent shed some light on the yield results. We therefore suggest that the use of as-rolled substrates is more appropriate for solar cell fabrication than the use of hardened SS substrates.

Table 3-8 shows only our most recent three runs. The six runs prior to these three runs show very similar results and are therefore omitted for inclusion in Table 3-8. Although the variation in J_{sc} for different types of cells is within measurement uncertainty at this moment, the data in Table 3-8 appear to indicate that 127 μm substrate provides a higher J_{sc} than the thin SS substrates. We believe that the difference, if any, would vanish after back-reflector layers, such as Ag/ZnO layers, are deposited on top of the surface.

We plan to put Ag/ZnO back-reflector and fabricate high-efficiency triple-junction solar cells on these ultra-thin SS substrates.

Taking the total thickness for the n, i, p and ITO layers to be 300 nm and that for the SS substrate to be 7.5 μm, the specific power for a 6.5% efficient solar cell (Gd480-1) becomes 1.08 kW per kilogram. Such a specific power can be further increased after we fabricate on these thin SS substrates triple-junction a-Si/a-SiGe/a-SiGe solar cells with around 11% efficiency, which have already been fabricated in our laboratory on 127μm thick substrates.[9,14] This high specific power is very important for space power application since it significantly reduces launching cost. In addition, a-Si based solar cells deposited on thin SS substrates can be easily rolled up thus reduce the cost associated with launching volume.

3.3.5 Conclusion

Amorphous silicon solar cells have been successfully fabricated on ultra-thin SS substrates with down to 7.5 μm in thickness. Using a carrier method throughout the fabrication process, we obtained ultra-lightweight solar cells that have similar performance as solar cells on regular 127 μm substrates, with a V_{oc} of 0.887 V, a J_{sc} of 10.8 mA/cm^2, a FF of 68% and an efficiency of 6.5% under AM1.5 illumination for cells deposited on bare SS without the use of a back-reflector. It should be noted here that the efficiency value under AM0 illumination should be approximately 20% lower than the efficiency measured under AM1.5 illumination. The solar cell efficiency could be further improved when a back-reflector is used and when a triple-junction solar cell is fabricated on these substrates. The solar cell yield, although slightly lower than those on thicker SS substrates, is however very promising. These 6.5% efficient solar cells deposited on 7.5μm thick SS substrates exhibit a specific power of 1.08 kW/kg, significant for space power application. We have studied the use of various types of SS substrates. The results we obtained so far appear to suggest that the as-rolled AISI316 SS foil is most suitable for the fabrication of a-Si based solar cells for space application.

3.4 Comparison study of a-Si and a-SiGe solar cells on glass and stainless steel

There are primarily two types of a-Si based solar cells being studied. One is n-i-p based solar cells deposited on stainless steel or Kapton substrates and the other is p-i-n based superstrate solar cells deposited on TCO coated glass. If is often found that these two types of solar cells do not perform closely, mainly due to two reasons: 1) that the growth of a-Si based materials depend sensitively on the substrates used, and 2) that the deposition sequence is opposite. To compare the difference between these two types of cells, we deposit n-i-p solar cells in the same deposition run on both SnO_2 coated glass and stainless steel substrates with and without Ag/ZnO back-reflector. Table 3-9 shows the performance of top, middle and bottom component cells deposited on different substrates. Both have n-i-p substrate type configuration, even for the device on glass. All measurements were taken with the light entering from the p-side.

We find that the V_{oc} and FF of n-i-p solar cells deposited on SS is somewhat higher than those on SnO_2 coated glass. We think that the small loss in V_{oc} may be from the interface between the n-layer and SnO_2 and the lowering of FF for the cells on glass is likely due to the resistance loss of SnO_2. The current of the cells on glass is close to the SS cells with back-reflector and much higher than the cells on bare SS. This is likely due to the efficient light trapping by the textured SnO_2 layer.

Table 3-9. Comparison of IV performance for a-Si top cell, a-SiGe middle cell and a-SiGe bottom cell deposited on SnO_2 coated glass and stainless steel.

Sample No.	Cell	Substrate	V_{oc} (V)	J_{sc} (mA/cm^2)	FF (%)	Eff (%)
GD459	Top	Glass/SnO_2	0.86	8.6	59	4.3
GD460	Middle	Glass/SnO_2	0.79	14.8	55	6.4
GD461	Bottom	Glass/SnO_2	0.60	16.6	44	4.4
GD485	Top	Glass/SnO_2	0.89	9.8	62	5.4
GD485	Top	SS	0.90	7.4	62	4.1
GD486	Middle	Glass/SnO_2	0.80	14.9	58	6.9
GD486	Middle	SS	0.81	13.2	61	6.5
GD488	Bottom	Glass/SnO_2	0.59	16.7	45	4.4
GD488	Bottom	SS/Ag/ZnO	0.66	20.5	54	7.3

3.5 Study of various p-layer deposition conditions for SS/n-i-p/ITO solar cells

For a-Si based solar cells, the window p-layer is very critical since it needs to be transparent to let light through to reach the absorber layer and it also needs to create a high built-in potential in the i-layer. A microcrystalline p-layer has demonstrated the advantage of being more transparent and provided higher built-in voltage than the amorphous counterpart. Microcrystalline p-layer is usually deposited under a high H dilution and high RF power. It is important to find the impact of the p-layer deposition conditions such as B doping, temperature and thickness on the solar cell performance.

We deposited p-layers of a-Si n-i-p solar cells under different conditions and compared the performance using quantum efficiency measurements under zero bias, forward bias and reverse bias. We use QE at 400nm to measure the p-layer optical transmission and the ratio of the QE measured under 0.7V forward bias to that measured under zero bias as an indication of p-layer electrical performance (similar to FF).

Table 3-10. List of p-layer deposited under different conditions and 400nm QE measured under different electrical bias for n-i-p solar cells with these p-layers.

p-layer conditions	Sample #	QE at 400nm	V(0.7)/V(0.0) at 400nm	V(0.5)/V(0.0) at 400nm	V(-0.5)/V(0.0) at 400nm
Standard @1Torr 70C	GD412	0.28	0.58	0.85	1.06
Std but 1/2 thick	GD411	0.45	0.56	0.94	1.04
Std but 2Torr	GD414	0.44	0.65	0.92	1.03
Std but 2x doping	GD415	0.35	0.21	0.60	1.06
Std but 1/2 doping	GD416	0.29	0.56	0.82	1.06
Std but 20C higher	GD417	0.32	0.57	0.84	1.08
Std but 40C higher	GD418	0.25	0.35	0.81	1.08

Figure 3-19 shows the QE curves for all of the samples measured under zero electrical bias. The sample with ½ thickness and the sample deposited at 2 Torr show the highest QE in the blue. Optically, a high QE at 400 nm indicates a highly transparent p-layer and that more light can reach the i-layer.

Figure 3-20 shows the QE curve of one typical sample measured under forward (0.5V and 0.7V) and reverse (-0.5V) bias. The QE under reverse bias is higher than that under no bias since the additional electrical field generated by the reverse bias enhances the collection of the light generated carriers. Under forward bias, the electrical field generated by the p-n junction is weakened by the bias, resulting in a reduced collection. The ratio of the QE measured under forward bias to that under zero bias correlates to the

FF of the solar cell devices. The reason that we are using QE rather than a solar simulator is that we could observe the "FF" properties for different wavelength of the incident light.

In Table 3-10, the QE at 400 nm and the QE ratio at 400 nm are summarized. Compared with the standard p-layer which is deposited at 1 Torr, 70 C, we find that

- p-layer with half the thickness is more transparent but slightly poorer FF.
- p-layer deposited at 2 Torr has the same transparency and has higher FF, probably due to higher microcrystalinity.
- p-layer deposited at temperature higher than standard is less transparent

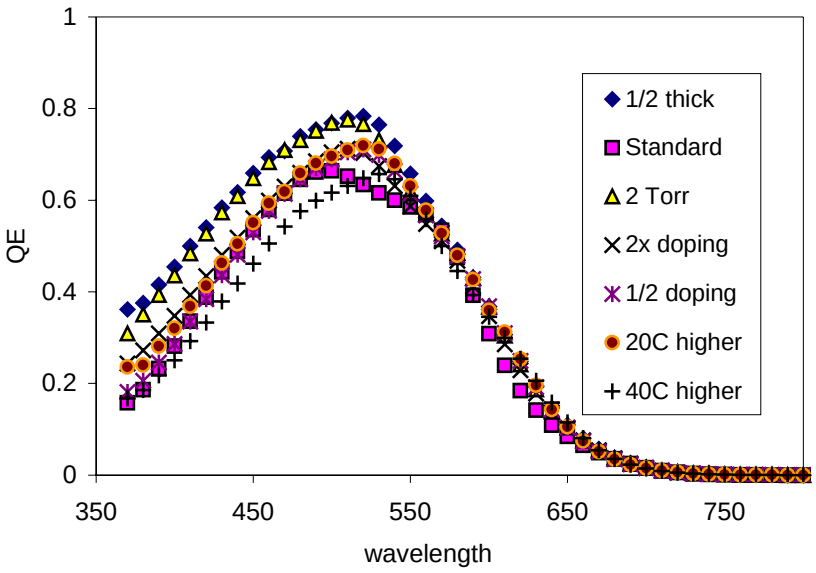

Figure 3-19. QE curves of n-i-p solar cells with different p-layers.

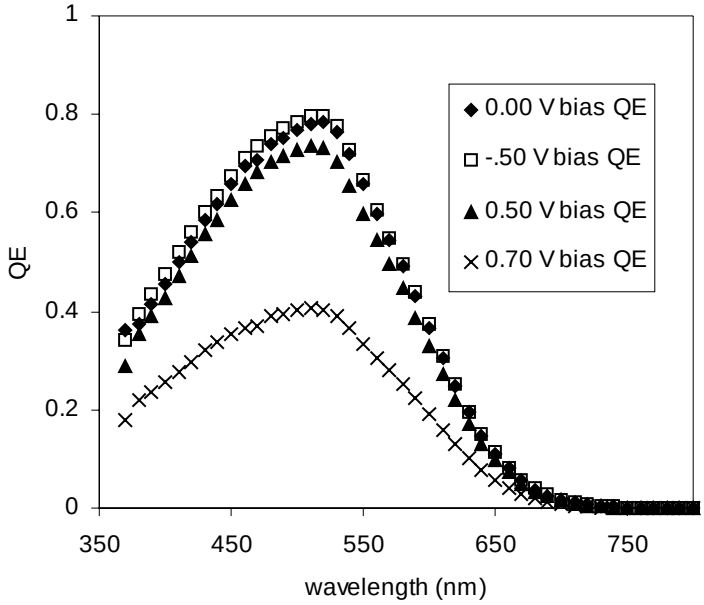

Figure 3-20. QE curves of one sample (GD411) measured under different biases.

3.6 Analysis of triple-cell current matching

The IV performance of a triple-junction solar cell depends sensitively on the current matching among the component cells that are connected in series within the triple cell. However, for a different solar spectrum, the matching could change slightly. Therefore, the matching, or mismatching, among the component cells depends on the location a cell or a triple-junction PV module is placed. To study the triple cell performance as a function of current matching, we fabricated a series of triple junction solar cells with different i-layer thicknesses (deposition times). We then observed the difference in the solar cell performance under a xenon arc lamp using IV and QE measurements.

In Table 3-11, three devices with different i-layer deposition times are listed. J-V performance is listed in the second block of columns. We also measured the quantum efficiency for the triple cells as shown in Figure 3-21. Integrating the QE values with the xenon lamp spectrum, which is very close to AM1.5 global spectrum, we calculated the short circuit current for the component cells under this particular light source. Current under AM1.5G is also calculated and is found to be close to the value under the simulator. On the right hand side of the Table 3-11, J_{sc} from QE for each component cell under UT's solar simulator is listed, while the total is shown in the last column.

From Table 3-11 and Figure 3-21, we made the following observations. The V_{oc} for all three devices are the same, as expected. The QE values indicate that the middle cell for GD489 is somewhat thin, given relatively low current. In sample GD491, the top cell is thinned down and middle cell is thickened, to boost the current of the middle cell. Indeed the top cell current is reduced due to reduced thickness. The middle cell current is increased due to 1) the reduced top cell thickness, hence allowing more light to the middle cell, and 2) increased middle cell thickness by taking more light from the bottom cell. We also find that the bottom cell current is slightly reduced. However, the sum of the current from all three component cells remains the same, at around 19.25 mA/cm2, since the bottom cell is unchanged. The intention of GD492 is to reduce the top cell thickness only without change the middle cell thickness, as compared with GD489. However, due to the small variation in the rf power, GD492 behaves very similarly as GD489.

Table 3-11. I-V and QE performance of triple-junction solar cells with different i-layer deposition times (thicknessses). The short circuit current on the right hand side of the table are calculated from the spectrum of the xenon solar simulator.

	i-layer dep time (min)			J-V performance			J_{sc} from QE using UT's simulator			
	Top	Middle	Bottom	V_{oc}	J_{sc}*	FF	Top	Middle	Bottom	Total
				(V)	(mA/cm^2)	(%)		(mA/cm^2)		
GD489	36	36	36	2.16	6.5	67	6.54	5.80	6.83	19.25
GD491	32	40	36	2.15	7.4	63	6.15	6.39	6.75	19.30
GD492	32	36	36	2.17	7.1	65	6.61	5.94	6.80	19.35

*) J_{sc} for these small 0.05 cm^2 solar cells has an uncertainty of 5-10%.

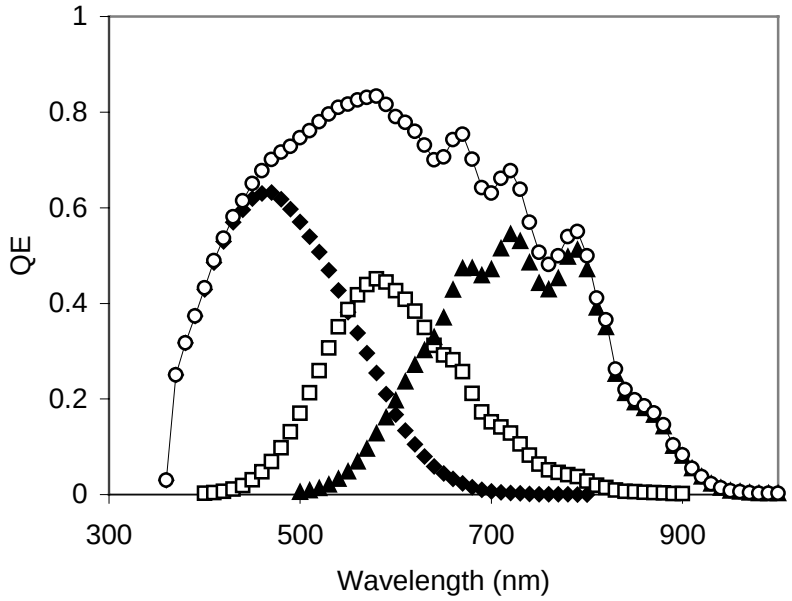

Figure 3-21. QE curve of a triple-junction solar cell GD489.

3.7 Acknowledgements

We would like to thank researchers at Energy Conversion Devices, Inc. and United Solar Systems Corp. for collaborations and assistance. In particular, we are grateful for helps provided by and discussions with Scott Jones, Tongyu Liu, Jeff Yang and Subhendu Guha.

3.8 References

1. L. Yang, L. Chen, and A. Catalano, MRS Proc. 219, 259 (1991).
2. J. Yang, X. Xu and S. Guha, MRS Proc. 336, 687 (1994).
3. M. Shima et. al, MRS Proc. 507, 145 (1998).
4. S. Guha, K.L. Narasimhan, and S.M. Pietruszko, J. Appl. Phys. 52, 859 (1981).
5. K. Tanaka and A. Matsuda, MRS Proc. 70, 245 (1986).
6. J. Yang and S. Guha, MRS Proc. 557, 239 (1999).
7. R. Swanepoel, *J. Phys. E: Sci. Instrum.* 16, pp. 1214-1222 (1983)

7a. Y. Chou and S. Lee, J. Appl. Phys. 83, 4111 (1998)

7b. E.V. Jelenkovic, K.Y.Tong, Z. Son, C.L. Mak, and W.Y. Cheung, J. Vac. Sci. Tech. A15, 2836 (1997)

8. J. Yang et al, *MRS Proc.* 149, 435 (1989)
9. X. Deng, X. B. Liao, S. Han, H. Povolny, P. Agarwal, *Solar Energy Mat. & Solar Cells*, **62**, 89 (2000)
10. J. Hanak, L. Walter, D. Dobias and H. Flasisher, “Deployable aerospace PV array based on amorphous silicon alloys”, Space Photovoltaic Research and Technology 1988, NASA Confference Publication 3030, April 1988.
11. G. Landis, S. Bailey and D. Flood, “Advances in thin-film solar cells for lightweight space photovoltaic power”, Space Power, Vol. 8. 31 (1989); available as NASA Technical Memo. TM-102017, 1989.
12. J. Woodyard and G. Landis, “Radiation resistance of thin film solar cells”, Solar Cells, Vol.31, 297 (1991).
13. S. Guha *et al*., “Amorphous silicon alloy solar cells for space applications”, 2nd World Conference on Photovoltaic Solar Energy Conversion, vol.3, 3609 (1998).
14. X. Deng, "Study of triple-junction a-Si alloy solar cells", in *AIP Conf. Proc.* 462, 297 (1998).

4.0 Publications

4.1 Refereed papers published or in press (3/99 – 3/00):

1. D. Grecu and A.D. Compaan, "Photoluminescence Study of Cu Diffusion and Electromigration in CdTe, Appl. Phys. Lett. **75**, 361-363 (1999).
2. A.D. Compaan, J.R. Sites, R.W. Birkmire, C.S. Ferekides, and A.L. Fahrenbruch, "Critical Issues and Research Needs for CdTe-Based Solar Cells," *Electrochemical Society Symposium Proceedings*, vol. 99-11, "Photovoltaics for the 21st Century" Seattle, WA, May, 1999.
3. Y.L. Soo, S. Huang, S. Kim, G. Kioseoglou, Y.H. Kao, A.D. Compaan, D. Grecu, and D. Albin, "Effects of heat treatment on diffusion of Cu atoms into CdTe single crystals," Appl. Phys. Letts. **76**, 3729 (2000).
4. D. Grecu, A.D. Compaan, D. Young, U. Jayamaha, and D.H. Rose, "Photoluminescence of Cu-doped CdTe and related stability issues in CdS/CdTe solar cells," J. Appl. Phys. **88**, 2490 (2000).
5. X.B. Liao, J. Walker, and X. Deng, "Effect of buffer layers in narrow bandgap a-SiGe solar cells," in *Amorphous and Heterogeneous Silicon Thin Fims—Fundamentals to Devices*, MRS Symp. Proc. **557**, 779 (1999).

4.2 Annual Subcontract Report:

1. Compaan, A. D.; Deng, X.; Bohn, R. G. (1999). High Efficiency Thin Film CdTe and a-Si Based Solar Cells: Annual Technical Report, March 4, 1998 - March 3, 1999. 68 pp.; NICH Report No. SR-520-27666. [Full manuscript available at http://www.nrel.gov/docs/fy00osti/27666.pdf]

4.3 Annual Contract Summary published in U.S. Dept. of Energy Photovoltaic Energy Program Contract Summary, FY 1999 [DOE/GO-102000-0976]:

1. A.D. Compaan and X. Deng, "High Efficiency Thin-Film Cadmium Telluride and Amorphous Silicon-Based Solar Cells," (Thin Film PV Partnership), p. 144.

4.4 Feature article for a trade journal:

1. Alvin Compaan, "Laser scribing creates nonolithic thin-film arrays," Laser Focus World, Jan. 2000, pp. 147-152. [Available on the web at www.optoelectronics-world.com. Search on Compaan. (Four color images.)]

5.0 Project Personnel

5.1 Visiting professors/scientists

Xianbo Liao

5.2 Postdoctoral Associates:

Kent Price
Sijin Han
Wenjing Wang

5.3 Graduate Students:

Greg Miller
M.S. completed August 1999

Chitra Narayanswamy
M.S. completed May 1999: "SIMS Analysis of Cu in ZnTe-Based Back Contacts for CdTe/CdS Solar Cells"

Xianda Ma
M.S. completed May 1999: "ZnTe:N Film as a Back Contact Material for Solar Cells"

Dan Grecu
M.S. completed 1998 (non thesis)
Ph.D.August 1999, “Photoluminescence Study of Cu-doped CdTe and Related Instability Issues for CdS/CdTe Solar-Cell Devices”

Ilvydas Matulionis
M.S. completed 1997 (non thesis)
Ph.D. in progress

Diana Shvydka
M.S. and Ph.D. in progress

Konstantin Makhratchev
M.S. completed June, 2000 (non-thesis)

Jennifer Drayton
M.S. in progress

Henry Povolny
Ph.D. in progress

5.4 Undergraduate and high school students

5.4.1 NSF Research Experiences for Undergraduates (REU) (summer 1999)

Adam Smith, Michigan State Univ.
Catherine Taylor, Westminster College, New Wilmington, PA

5.4.2 Research Experiences for Teachers

David Simmons, St. John's Jesuit High School, Toledo, OH

5.5 Technical Assistant

Robert Burmeister (4/96-) (25% time)